Complex motion of Greenland Ice Sheet outlet glaciers with basal temperate ice

Robert Law – rl491@cam.ac.uk, @_Rob_Law

Poul Christoffersen – pc350@cam.ac.uk

Emma 'Mickey' MacKie – emackie@ufl.edu

Samuel Cook – samuel.cook@univ-grenoble-alpes.fr

Marianne Haseloff – marianne.haseloff@northumbria.ac.uk

Olivier Gagliardini – olivier.gagliardini@univ-grenoble-alpes.fr

FRONT MATTER

Title

Complex motion of Greenland Ice Sheet outlet glaciers with basal temperate ice
Complex basal motion of the Greenland Ice Sheet

Authors

R. Law[1]*, P. Christoffersen[1], E. MacKie[2], S. Cook[3], M. Haseloff[4], O. Gagliardini[3]

Affiliations

[1]Scott Polar Research Institute, University of Cambridge; Cambridge, UK.

[2]Department of Geological Sciences, University of Florida; Gainesville, Florida, USA.

[3]CNRS, IRD, Grenoble INP, IGE, Université Grenoble Alpes; Grenoble, France.

[4]Department of Geography and Environmental Sciences, Northumbria University; Newcastle, UK.

*Corresponding author: rl491@cam.ac.uk

Abstract

Uncertainty associated with ice motion plagues sea-level rise predictions. Much of this uncertainty arises from imperfect representations of physical processes including basal slip and internal ice deformation, with ice-sheet models largely incapable of reproducing borehole-based observations. To investigate further, we model isolated 3D domains from fast-moving (Sermeq Kujalleq or Store Glacier) and slow-moving (Isunnguata Sermia) ice-sheet settings in Greenland. By incorporating realistic geostatistically simulated topography, we show that a layer of basal temperate ice (much softer ice at the pressure-melting point) with spatially highly variable thickness forms naturally in both settings, alongside ice-motion patterns which are far more complex than previously considered. Temperate ice is vertically extensive in deep troughs, but thins notably over bedrock highs. Basal-slip rates are interconnected with this variability, reaching >90% or <5% of surface velocity dependent on setting. This realistic representation of ice-sheet motion opens new pathways for improving parameterizations in large-scale ice-sheet models.

Teaser

Geostatistically realistic topography forces complex patterns of basal slip and deformation in Greenland outlet glaciers.

MAIN TEXT

Introduction

The Greenland Ice Sheet (GrIS) has transitioned from a state of near zero mass balance in the 1990s to large and sustained (>200 Gt a^{-1}) annual mass losses since the mid-2000s, and is now the largest cryospheric contributor to sea-level rise (*1*). While the satellite era has greatly increased the accuracy of mass-balance observations, model predictions for future ice loss remain highly uncertain (*2*, *3*), but indicate substantial and non-linear sea-level rise under future anthropogenic warming (*4*–*7*). Ice dynamics, and their parameterization for large ice-sheet models (*8*–*12*), are crucial components of this uncertainty, being responsible for ice transport to lower and warmer elevations where surface melt rates and runoff increase rapidly, and to the fronts of marine-

terminating glaciers where ~50% of GrIS net annual mass loss occurs through increased calving rates and discharge (*13*).

Uncertainty related to ice-sheet motion arises from inadequate understanding of its two major components: (i) basal-slip at the ice-sediment or ice-rock interface and (ii) deformation within the ice sheet itself. State-of-the-art GrIS models run with BedMachine, the most advanced gridded data product of GrIS basal topography which is relatively smooth compared to deglaciated terrain (*14*, *15*), produce basal-slip and ice deformation rates that vary smoothly and are largely independent of one another [e.g. (*4*, *16*, *17*)]. However, GrIS borehole records indicate substantial variation in ice deformation, particularly towards the ice-sheet bed (*18–21*) and notable catchment-scale variations in the thickness of a much softer, and relatively poorly understood, basal temperate layer in which ice co-exists with a liquid water phase at the pressure-dependent melting point (*22*, *23*). Here, we advance upon 2D models that begin to unpick this complexity (*19*, *24*) by incorporating realistic three-dimensional geostatistically simulated bed topography (Fig. 1) and improved temperate ice rheology in a 3D full-Stokes model (Fig. 2A). We focus on ice-motion at the previously overlooked intermediate scale (≥25 m, ≲4 km), bridging recent advances in understanding at small (*25*, *26*) and large (*17*) scales. The outcomes explain why field observations can be highly variable over even short distances. This behavior is characterized by spatially complex patterns of modeled ice deformation – focused towards the ice-sheet bed – and basal-slip. The basal temperate layer is an important modulator, extending or compressing in response to topographic perturbations, with vertical gradients in ice velocity notably reduced just above the cold-temperate transition surface (CTS). We suggest that this improved understanding will enable more accurate parameterizations of ice sheet motion at large-scales and hence lead to more accurate predictions of sea-level rise in the coming decades and centuries.

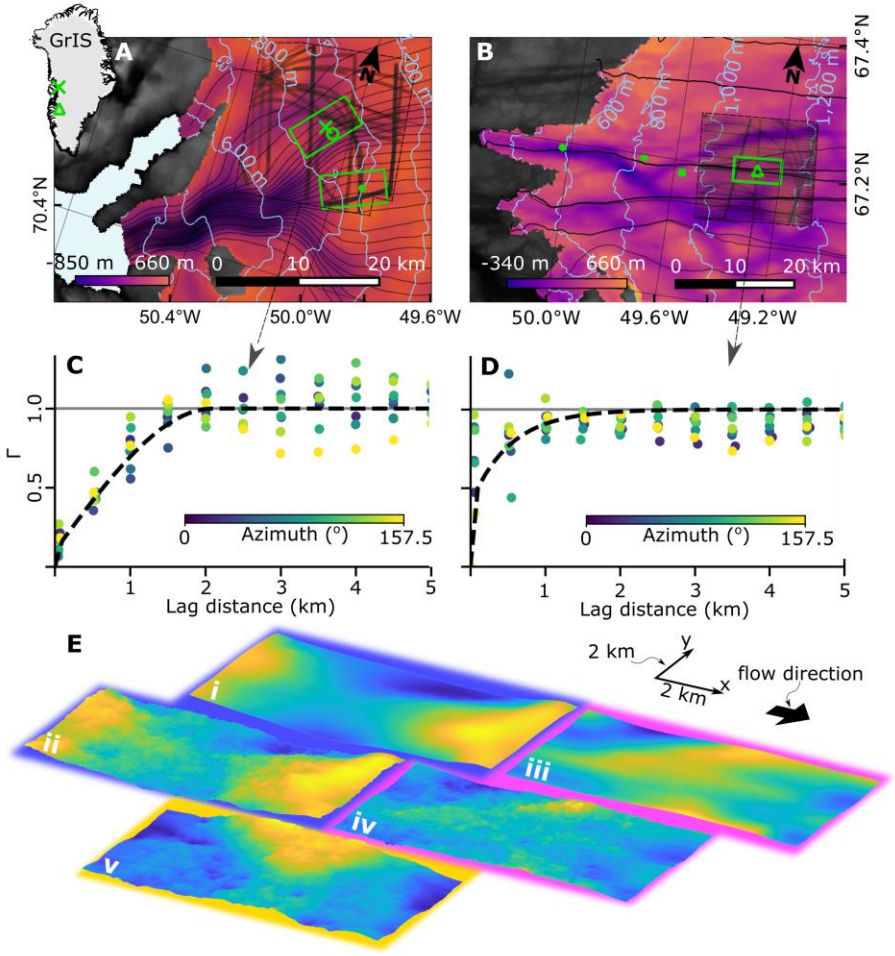

Fig. 1. Location of modeling domains, variograms, and model setup. (**A**) Sermeq Kujalleq (Store Glacier) showing flowlines in black converging into Uummannaq fjord. BedMachine v3 (*14*) basal topography (inferno colormap), land topography (grayscale), and ice surface contours (pale blue). Model domain locations containing RESPONDER (north fluorescent green rectangle), borehole BH19c location [fluorescent green cross (*23*)], borehole BH18c location [fluorescent circle (*27*)]; SAFIRE domain (south fluorescent green rectangle), borehole BH14b-c location [fluorescent green dot (*28*)] and radar flight lines for RESPONDER domain [bold black strokes within dashed boundary, scatter opacity means darker lines have more measurements, (*29*)]. (**B**) As for **A** but Isunnguata Sermia showing the S5 domain (fluorescent green rectangle) and boreholes S5 (fluorescent green triangle), S4 (west fluorescent green dot), S2 (east fluorescent green dot), and IS2015 [fluorescent green square (*19*)]. S2-S5 are from (*30*). (**C**) Modeled variogram (dashed line) and empirical variograms for varying azimuths (points) for RESPONDER domain, see Fig. S1 for SAFIRE variogram and flight lines. Variograms describe the spatial statistics of measured topography. (**D**) As for **C** but for Isunnguata Sermia domain. (**E**) BedMachine (i and iii) and geostatistically simulated (ii, iv, and v) basal DEMs for RESPONDER (blue outline), Isunnguata Sermia (pink outline), and SAFIRE (yellow outline) domains. Flow direction and x y scale in top right. No vertical exaggeration used.

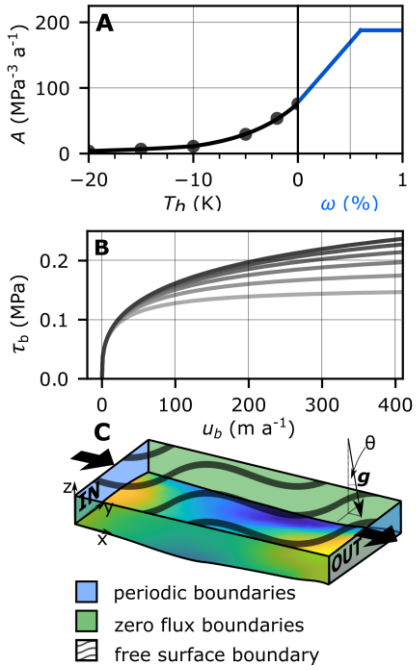

Fig. 2. Ice rheology, basal traction, and periodic setup. (**A**) Rate parameter, A, as a function of homologous temperature (temperature below the melting point, black line) and water content (blue line). Black dots show values from (*31*). (**B**) Regularized-Coulomb relationship with $F = 1.2$, $s - b = 1{,}043$ m, $C = 0.1617$, and $\theta = 0.8\text{-}1.8^{o}$ in 0.2^{o} increments (see Materials and methods for equation and symbol definition). (**C**) (Periodic) model setup showing inflow and outflow boundaries (labelled IN, OUT) with RESPONDER BedMachine topography (MatLab parula colormap), axis orientation, zero-flux lateral boundaries, free surface, and gravity vector.

Results

Our modeling approach explores ice motion in isolated domains across three distinct glaciological settings. Two domains are from the fast-moving (~500 m a^{-1}) Sermeq Kujalleq (or Store Glacier, Fig. 1A), which flows into Uummannaq Fjord in West Greenland. The RESPONDER simulation

is centered on the 1,043 m deep RESPONDER project borehole BH19c (*23*) drilled at the center of a drained lake above a basal topographic saddle (Figs. 1Ei, ii). The SAFIRE simulation is centered on the 611 m deep SAFIRE project borehole BH16c (*28*), which measures ice motion over a contrasting ~300 m bedrock rise (Fig. 1Ev). The third simulation, S5, is centered over the ~818 m S5 borehole site from (*30*) on the slow-moving (<125 m a^{-1}) land-terminating Isunnguata Sermia (Fig. 1B, Eiii, Eiv) where there are no substantial large-scale topographic troughs or rises.

All domains are run using geostatistically realistic topography (produced at a horizontal resolution of 20 m) using the sequential Gaussian simulation method. This well-established procedure treats topography as a Gaussian process, thereby matching airborne radar measurements of bed elevation along flight-lines exactly, while also reproducing the roughness characteristics observed along flight-lines (Materials and methods). The RESPONDER and S5 domains are additionally run using 400 m horizontal resolution BedMachine v3 topography to assess the difference in ice-motion behavior resulting from the two topographic approaches. In the areas around our domains, BedMachine is derived from interpolated radar flight lines taking into account mass conservation (*32*). While this methodology is a substantial improvement over earlier kriging interpolation, the resulting topography product is still considerably smoother than topography observed along radar flight lines (*33*). We achieve a close fit between modeled and observed surface velocity in a two-step approach. First, the ice rheology is set from a prescribed vertical temperature profile based on borehole data and the slope of the ice slab is adjusted to match the observed surface velocity (Fig. 2C, Table S1). Subsequently, we incorporate thermomechanical coupling while keeping the surface and inflow boundary conditions fixed. Basal-slip is calculated using a regularized-Coulomb relationship which parameterizes complex small-scale (<25 m) behavior such as cavitation (*26*) and sediment ploughing [Fig. 2C, (*25*)]. This avoids a basal-traction inversion procedure which masks basal variation at sub ice-thickness scales (Materials and methods).

Ice motion through a topographic saddle (RESPONDER domain)

When forced with geostatistically simulated topography (run Rgb, Figs. 3, 4, table S1), basal-slip rates, internal deformation, and the thickness of the basal temperate layer show great variation across the entire RESPONDER domain, forming a clear contrast to lower variation in the BedMachine topography model output (run Rbm, Fig. 4). With geostatistically simulated topography, the basal temperate ice layer is vertically extensive (>90 m) in topographic depressions, with low basal slip rates (<15 m a^{-1}) while fast (~500 m a^{-1}) surface velocity shows no local variation. However, the basal temperate ice layer thins dramatically (<10 m) over topographic highs, with fast basal-slip rates (>500 m a^{-1}, Figs. 3A, B, pink and white rings respectively). To explore the transition from cold to temperate ice we track deformation heat and water content changes in flowlines originating ~60 m above the bed 3 km along the x axis (Fig. 3E). These show transitions from cold ice with no water content to temperate ice with the maximum allowable water content of 2.5% (Materials and methods) over distances as short as ~0.5-3 km (Fig. 3C) due to intense internal heat dissipation caused by the movement of ice over topographic obstacles (Fig. 3C pink and white rings). Deformation heating is notably lower within cold ice regions where ice is stiffer, than in the temperate basal layer where ice is much softer (Fig. 2A, Figs. 3C, D white line). Large topographic obstacles also divert ice flow horizontally (Fig. 3F, white ring) as well as vertically (Fig. 3E), thereby influencing the vertical position of the cold-temperate transition surface (CTS) and rheological properties throughout the domain. The ice-sheet (free) surface, with a surface elevation change of 98 m, varies broadly in response to patterns in BedMachine topography, with similar trends across all RESPONDER runs (Fig. S2). ParaView output files for all runs across all domains are available in the supplementary material.

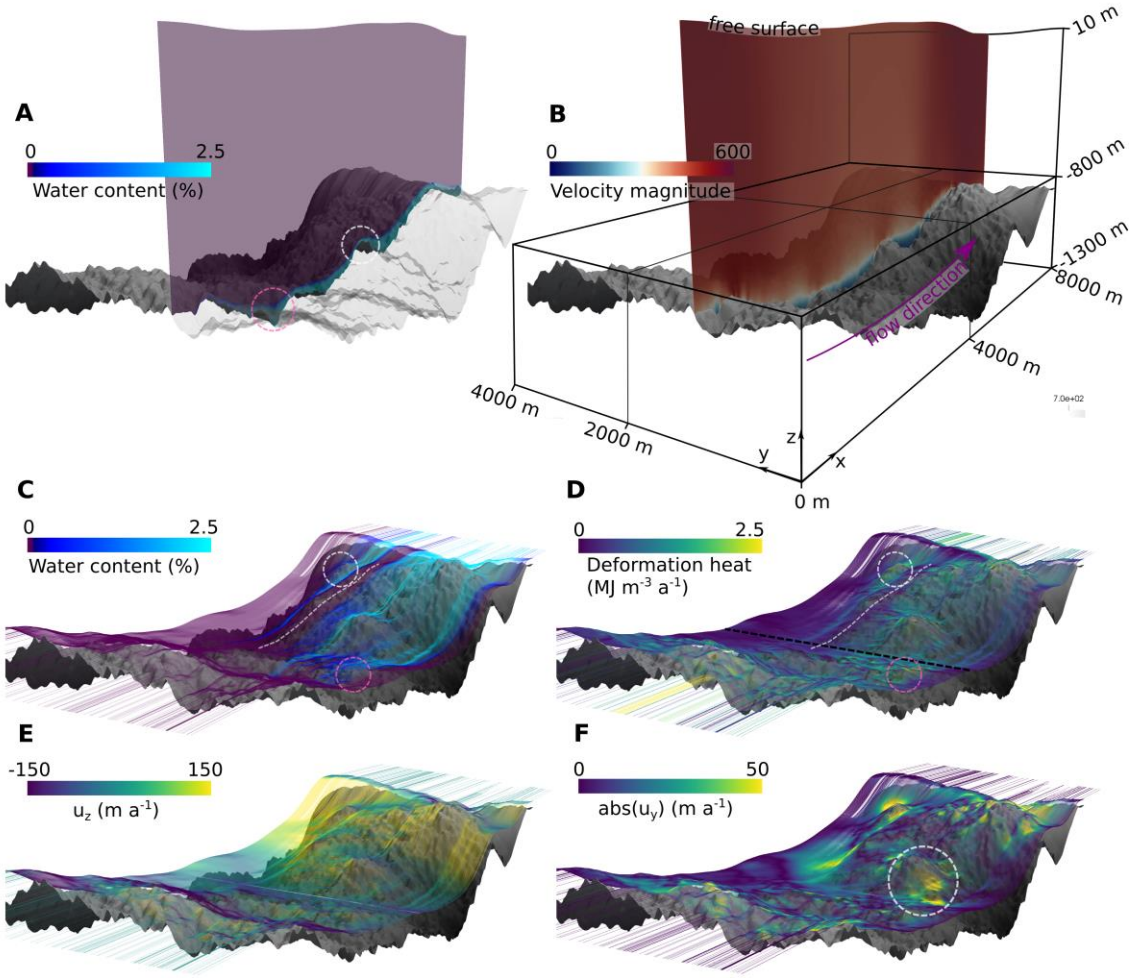

Fig. 3. 3D model output from RESPONDER geostatistical simulation (Rgb)**.** Flow direction is left to right, basal topography is in gray (max and min elevations are -835 and -1349 m respectively). z axis is exaggerated by a factor of 3. (**A**) shows water content and temperate ice thickness along xz transect intersecting y coordinate 1,300 m (same plane as **Fig. 4**). Transparency applied to topography on the observer's side of the transect. (**B**) Transect as for **A** showing velocity magnitude with flow direction in pink, axis orientation and dimensions visible. (**C**) Water content mapped onto 750 flowlines originating at line with coordinates [(3000, 0, -1083.3), (3000, 4000, -1083.3)] shown as black dashed line in **D**. (**D**) As for **C** but with deformation heat. Pink dashed ring highlights high but variable deformation heating where particles are close to the base over rough topography. White dashed ring highlights high deformation heating over a topographic prominence. White dashed line highlights an area of cold ice with low deformation heating. (**E**) As for **C** but z component of velocity vector mapped onto flowlines. (**F**) As for **C** but magnitude of y component of velocity vector mapped onto flowlines. White ring highlights region of high abs(u_y) around an area of high topographic prominence.

Deformation heating profiles for BedMachine (run Rbm) and those from geostatistically simulated topography (run Rgb) are markedly distinct (Fig. 4A, B). When forced with geostatistically simulated topography the basal velocity ratio – the basal-slip rate divided by the surface velocity – reaches a maximum of 0.86 on a topographic high (Fig. 4C, gray line), where internal deformation drops rapidly above the bed. The basal velocity ratio is smallest within a topographic depression (0.04), where the deformation rate reaches its peak value (5.5 a^{-1}) just below the CTS, 90 m above the bed (Fig. 4C, brown line). The CTS velocity ratio – the velocity at the CTS divided by the surface velocity – remains more uniform throughout, peaking over

topographic prominences but not dropping below 0.5 (Fig. 4E). Profiles also show deformation rates increasing upwards (Fig. 4C blue line), downwards (Fig. 4C yellow line), or even alternating between both (Fig. 4C red line, 1 km). Strain banding towards the top of the temperate zone is evident in several locations, but is not a continuous feature across the entire domain. Distinctive vertical and horizontal banding in deformation heating is seen predominantly within the temperate layer (close-up in Figs. 4G-J, expanded upon under Temperate ice deformation-heating behavior). Basal melting varies with basal-sliding (Fig. 4F) but removes basal temperate ice at around 1.3 m km^{-1}, making it an important, but not first-order, control on temperate-layer thickness in the RESPONDER domain.

The above behavior contrasts the uniform ice-motion produced when the model is run with BedMachine topography (Fig. 4A), which gives deformation profiles that are uniform in shape throughout the model domain (Fig. 4B) that broadly conform with deformation profiles obtained from assumptions of plane-strain [e.g. (*20*)]. The thin temperate zone, increasing gradually and uniformly along the transect, accommodates the largest rates of internal deformation (~3 a^{-1}) with a monotonic decrease in the ice above. The basal velocity ratio remains high and relatively uniform across the transect with an average value of 0.72.

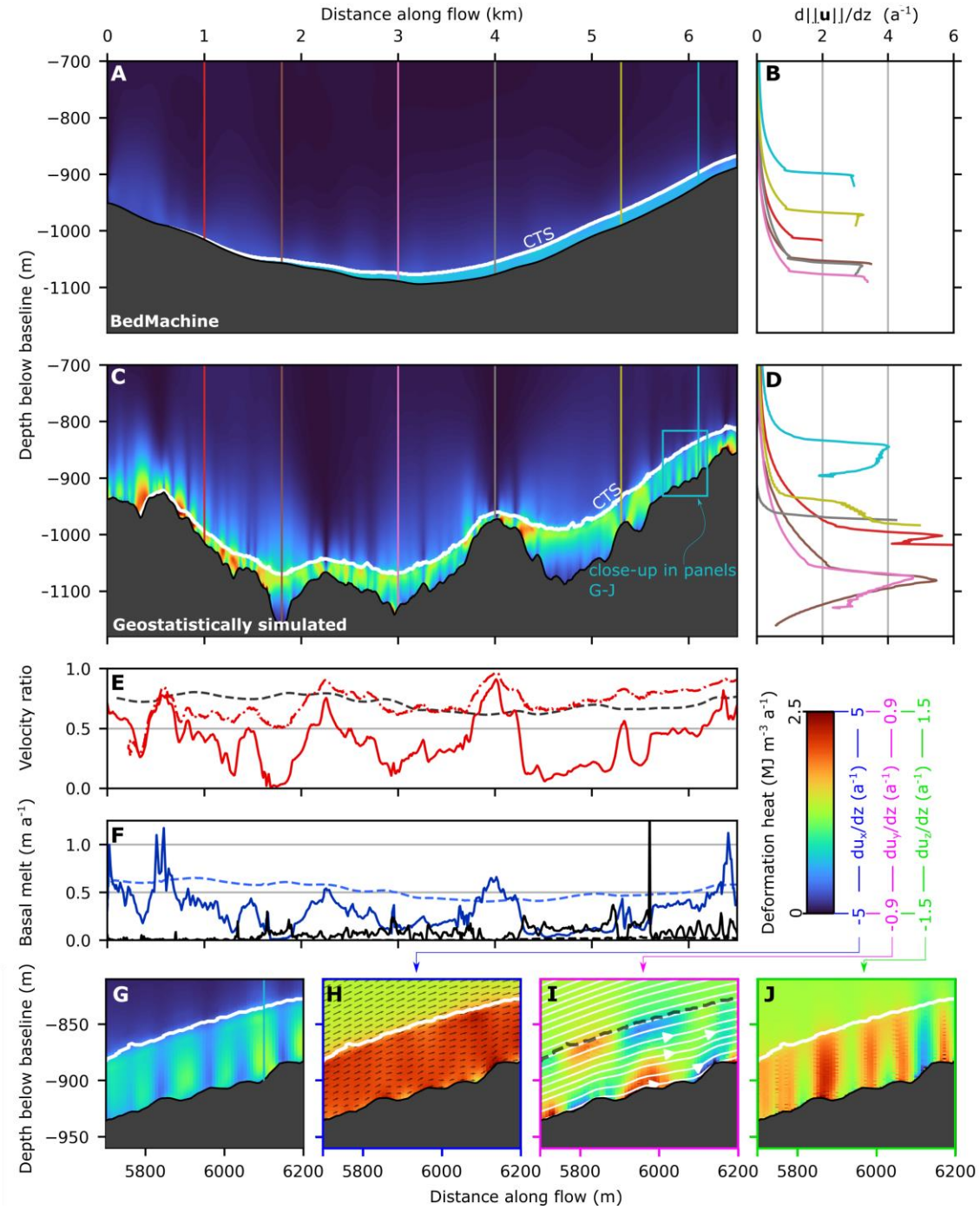

Fig. 4. RESPONDER cross section (Sermeq Kujalleq). Cross section in xz plane showing deformation heat (product of stress and strain matrices) at y = 1,300 m (the same y value as the transects in Fig. 3) for (**A**) BedMachine topography (run Rbm) and (**C**) geostatistically simulated topography (run Rgb). Panels (**B**) and (**D**) show deformation rate profiles (change in velocity magnitude with depth) with colors and depths corresponding to the vertical lines in panels (**A**) and (**C**). (**E**) shows the basal velocity ratio (basal velocity magnitude divided by surface velocity magnitude) for Rbm (dashed line) and Rgb (solid line) along the transect and CTS velocity ratio (velocity magnitude at CTS divided by surface velocity magnitude) for Rgb (dashed black line). (**F**) shows basal melt rate in blue and drainage from temperate ice in black for Rbm (dashed line) and Rgb (solid line). Lowermost panels are the close up in **C** for Deformation heat (**G**), change in x-oriented velocity with depth (**H**), change in y-oriented velocity with depth (**I**), and change in z-oriented velocity with depth (**J**). Colored lines from left to right at 1.0, 1.8, 3, 4, 5.3, and 6.1 km.

Colored lines in this figure, and Figs. 5 and 6, are chosen to highlight interesting deformation behavior.

Ice motion over a bedrock rise (SAFIRE domain)

At the SAFIRE domain, geostatistically simulated topography (Fig. S1) again results in highly variable basal-slip rates, ice deformation, and temperate-layer thickness (Fig. 5). The temperate layer thins over the large topographic rise in the domain, with a notable increase in basal velocity ratio (Fig. 5A between red and mauve lines). Over the rise, the basal velocity ratio is high (up to 0.98, Fig. 5A yellow line), but remains highly variable dropping to a minimum of 0.38 (Fig. 5A orange line). The CTS velocity ratio still shows obvious variation, but is much more uniform across the domain than the basal velocity ratio, and only rarely drops below 0.5. Deformation profiles show as much variability as in the RESPONDER simulation, however rates are higher and more spatially concentrated. Basal melt rates are directly correlated with basal slip rates (Fig. 5C, D) and drainage from temperate ice is low throughout, increasing on the lee side of the rise to a maximum of 0.22 m a^{-1}.

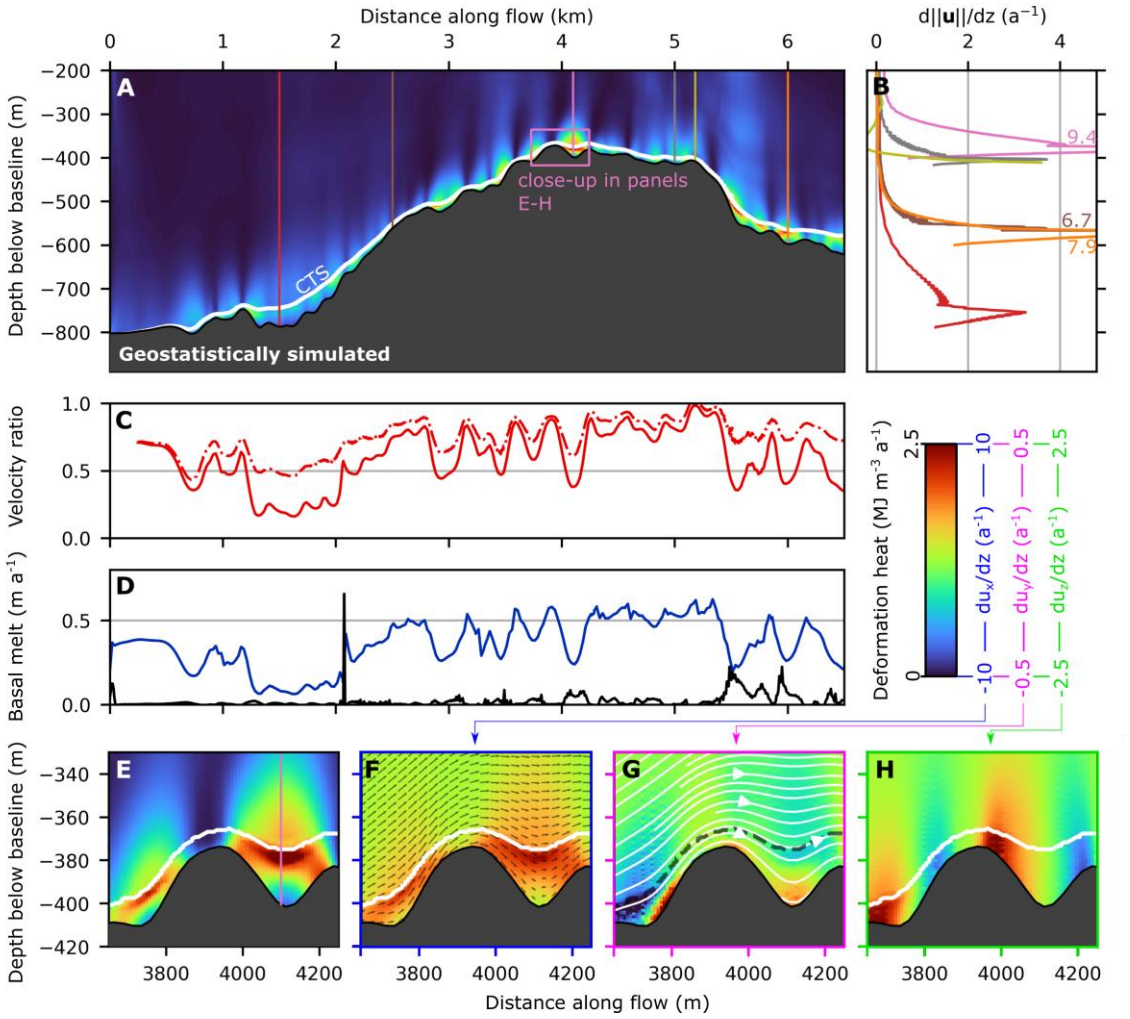

Fig. 5. SAFIRE cross section (Sermeq Kujalleq). Cross section in xz plane at y = 2,850 m for (**A**) geostatistically simulated topography (run SAFg). The remainder of the figure follows the same layout as **Fig. 4**. Colored lines from left to right at 1.5, 2.5, 4.1, 5, 5.18, and 6 km.

Ice motion at a land-terminating margin (S5 domain)

Ice motion and temperate ice behavior at the S5 Isunnguata Sermia site with geostatistically simulated topography are once again notably distinct from other domains, forced by increased short wavelength (<500 m, Fig. 1D) roughness, reduced topographic perturbations at larger (≳2 km) scales, and lower surface velocity. Along the featured transect (Fig. 6C), the basal velocity ratio remains mostly above 0.5 and does not have the same precipitous drops exhibited in the Sermeq Kujalleq domains. High basal velocity ratios (up to 0.83) still occur at topographic prominences, but compared to the Sermeq Kujalleq domains the CTS velocity ratio shows less departure from the basal velocity ratio, particularly in the first half of the transect where the basal temperate ice layer is thinner (<40 m). Deformation heat is less obviously concentrated towards the top of the temperate zone, instead projecting upwards through the CTS and well into the cold ice ~150 m above the bed (close-up in Figs. 6G-J). Nevertheless, most deformation profiles for geostatistically simulated topography show deformation rates increasing to a maximum just below the CTS, except over some topographic prominences (e.g. Fig. 6D, red line), where deformation decreases monotonically above the bed, as is the case for all deformation profiles for the BedMachine run (Fig. 6B). BedMachine topography produces similar features to the Sermeq Kujalleq BedMachine domains: a gradual temperate layer thickness increase and internal deformation concentrated within the temperate layer.

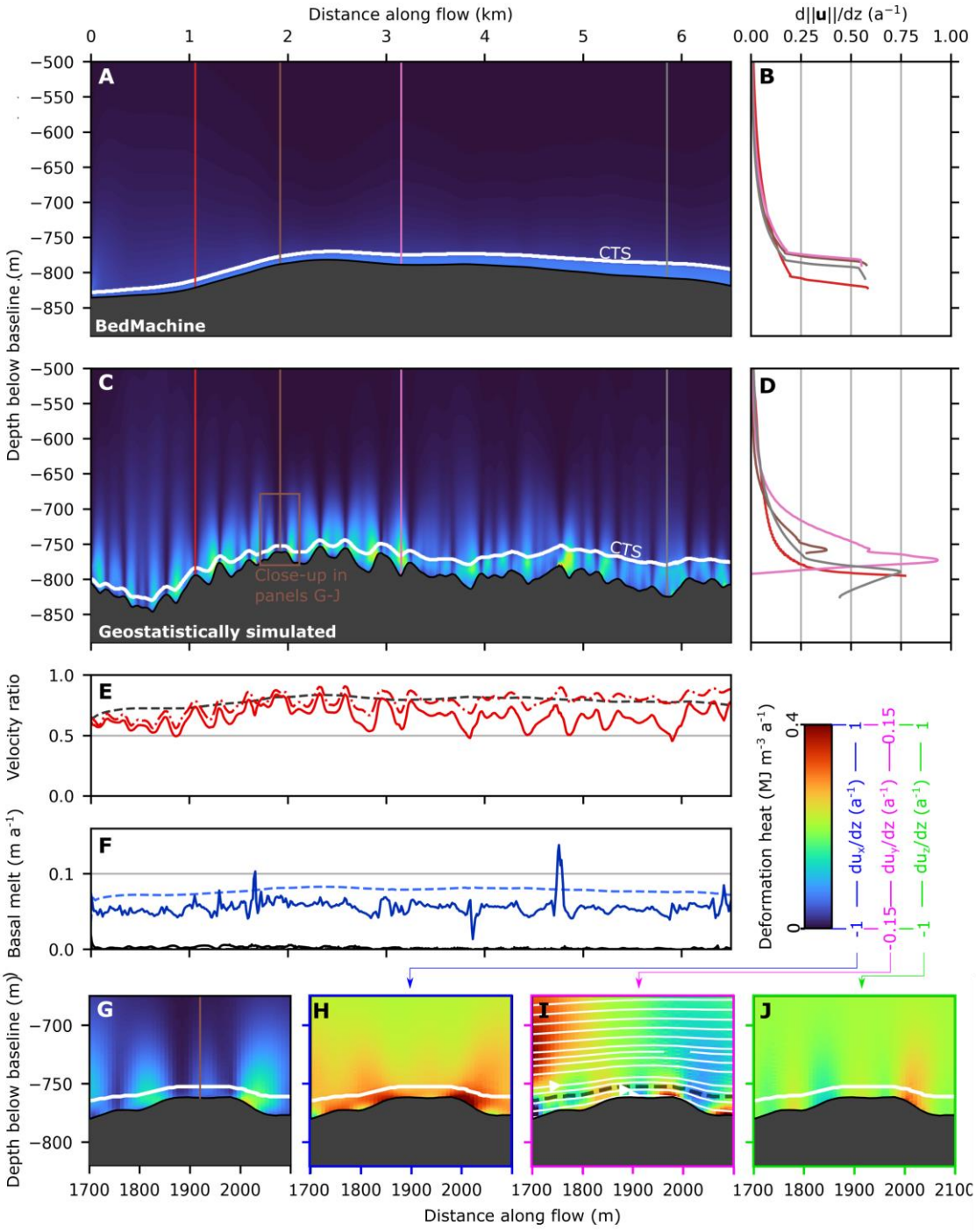

Fig. 6. S5 cross section (Isunnguata Sermia). Cross section in xz plane at y = 2,000 m for (**A**) BedMachine topography (run S5bm) and (**B**) geostatistically simulated topography (run S5gb). The remainder of the figure follows the same layout as **Fig. 4**. Colored lines from left to right at 1.06, 1.92, 3.15, and 5.85 km.

Temperate ice deformation-heating behavior

We observe three characteristic patterns of deformation heating. First 'Truncated spires' (e.g. Figs. 4G-J) refers to places where deformation heating is evident in vertically oriented bands (~50 m across) that terminate abruptly below the CTS. These truncated spires are connected to changes in x-oriented velocity with depth (Fig. 4H) and are more frequent as temperate-layer thickness

increases. This pattern of deformation heating is common in both Sermeq Kujalleq domains but is largely absent in the Isunnguata Sermia S5 domain. 'Bridges' (e.g. Figs. 5E-H) are another characteristic feature. Here a deformation heating arch below the CTS and above a topographic depression is produced by large changes in x-oriented velocity with depth (Fig. 5F). Bridge abutments are produced as the temperate layer vertically extends and depth-averaged velocity decreases on the lee side of a prominence before vertically compressing with an increase in depth-averaged velocity as the trough is exited. Bridges are also common in both Sermeq Kujalleq domains but are mostly absent in the S5 domain. Last, 'crosscutting spires' or simply 'spires' (e.g. Figs. 6G-J) are similar to truncated spires but protrude some distance (~100 m) above the CTS, gradually reducing in intensity with height. Spires are the most common feature in the Isunnguata Sermia domain but are also common in the two Sermeq Kujalleq domains in locations where the temperate layer is thinner. These features are outlined in further detail in the discussion and used singularly without 'deformation-heating' from here on.

Domain-wide behavior

Domain-wide distributions of basal-velocity ratio and temperate-layer thickness show substantial variation between locations and are further highly dependent upon whether BedMachine or geostatistically simulated topography is used (Fig. 7, fig. S3). Runs from Sermeq Kujalleq domains with geostatistically simulated topography exhibit the greatest range in basal velocity ratios, with 1st and 99th percentile values of 0.04 (0.05) to 0.80 (0.92) for RESPONDER and (SAFIRE) respectively. This far exceeds results when BedMachine topography is used (1st and 99th percentile values of 0.43 and 0.86 respectively for the RESPONDER BedMachine run). Modal basal velocity when geostatistically simulated topography is used varies from 0.31 for RESPONDER, to 0.60 at S5 and 0.71 at SAFIRE, with the trend reversed for modal temperate ice thickness (49 m for RESPONDER, 17 m for S5, and 12 m for SAFIRE) and a maximum temperate ice thickness of 189 m modeled in the RESPONDER domain. Each hexbin plot for geostatistically simulated topography has a central 'hotspot' that clearly varies between domains, with the spread around the hot spot showing a broad linear relationship between basal velocity ratio and temperate ice thickness. In contrast to all of the geostatistical runs, the RESPONDER BedMachine hexbin plot (Fig. 7D) is much closer to a line. In runs using geostatistically simulated topography, the temperate ice layer thickness only shows a linear increase along flow in the flatter S5 Isunnguata Sermia domain, with average temperate-layer thickness increasing to a maximum that coincides with the topographic minima in the RESPONDER domain, and increasing overall but with no consistent trend in the SAFIRE domain.

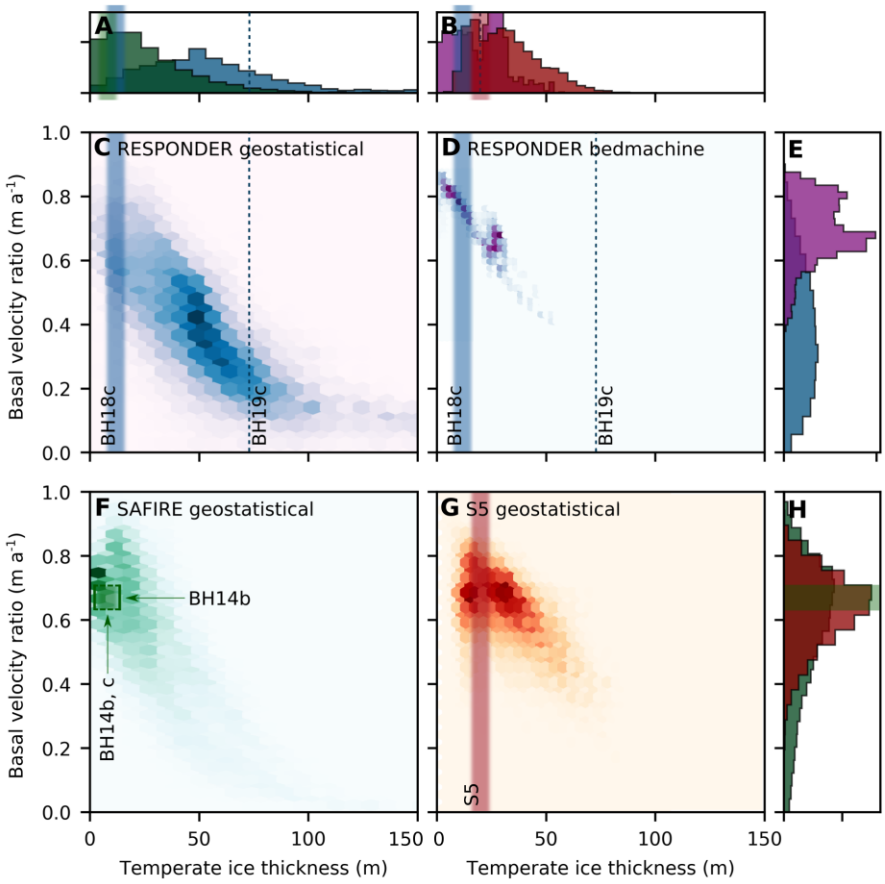

Fig. 7. Domain-wide distributions of basal velocity ratio and temperate ice thickness. (**A**) Histograms for temperate ice thickness for RESPONDER and SAFIRE geostatistical domains. (**B**) Histograms for temperate ice thickness for RESPONDER BedMachine and S5 geostatistical domains. (**C**, **D**, **F**, **G**) Hexbin plots for temperate ice thickness and basal velocity ratios for (**C**) RESPONDER geostatistical domain (run Rgb, modal bin has 420 counts), (**D**) RESPONDER BedMachine domain (run Rbm, modal bin has 582 counts), (**F**) SAFIRE geostatistical domain (run SAFg, modal bin has 755 counts), and (**G**) S5 geostatistical domain (run S5gb, modal bin has 463 counts). (**E**, **H**) Histograms for basal velocity ratio for RESPONDER geostatistical and BedMachine domains (**E**) and SAFIRE and S5 geostatistical domains (**H**). Vertical (**A, B**) and horizontal (**E,** H) histogram axes are frequency density. A buffer of 500 m, with an additional 1,000 m at the outflow boundary is applied around domain edges to avoid potential boundary effects, giving a total of 34,677 points per domain. Dashed blue line indicates temperate ice thickness recorded at BH19c, the distributed nature of this measurement means there is negligible uncertainty. The vertical green, blue, and red bars for BH14c (*28*), BH18c (*27*), and S5 (*30*) respectively are blurred to indicate uncertainty due to discrete temperature sensor measurements which may miss the exact location of the CTS. Uncertainty bounds are not provided in the original papers and we do not attempt to create our own. The green horizontal bar (not blurred) spans the uncertainty range of 0.63-0.71 (*28*). The complex basal motion in our model is supported by borehole observations from within each of the three domains (see main text for details).

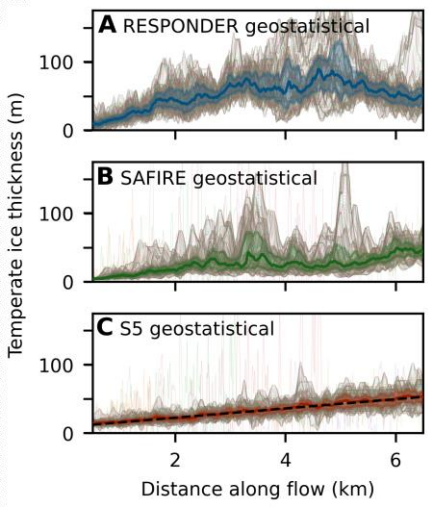

Fig. 8. Temperate ice thickness along flow. Temperate ice thickness interpolated into a 5 m orthogonal grid from output triangular mesh. Gray lines are temperate ice thickness for each y value along x-axis-parallel rows. Highlighted area bounds interquartile range obtained for each y-axis-parallel column, solid colored line is 50% percentile for each y-axis-parallel column. (**A**) RESPONDER geostatistical domain (run Rgb). (**B**) SAFIRE geostatistical domain (run SAFg). (**C**) S5 geostatistical domain (run S5gb) where the black dashed line is the first order polynomial fit of the 50% percentile line.

Our numerical findings demonstrate that geostatistically realistic topography produces basal-slip and internal deformation rates that conform to a broad uni-modal distribution. Borehole observations will sample the *actual* distribution of basal velocity ratio and temperate-layer thickness, but are too limited in number to be used to produce a statistically 'correct' distribution. Nonetheless, our model shows good agreement with borehole observations for all runs with geostatistically simulated topography, matching modal values for temperate ice thickness for SAFIRE and S5. Observed temperate-layer thickness falls either side of the mode for RESPONDER with geostatistically simulated topography, confirming such spread is present in the GrIS. Given that the observed temperate layer thickness of 73 m at BH19c (*23*) is entirely outside of the distribution produced with BedMachine topography, we argue that realistic topography is a requirement for realistic temperate-layer thicknesses and therefore also realistic basal motion.

Discussion

In contrast to the smoothly varying velocity fields produced by most ice-sheet models using BedMachine topography, our simulations indicate that basal-slip and internal deformation are pervasively heterogeneous, with significant variability over sub-kilometer distances, and across disparate catchment settings. In this discussion, we first detail the mechanisms that produce and shape the temperate layer which has a central role in fast ice motion, before outlining the processes behind the complex basal-motion patterns simulated in our model. Both of these aspects are separately compared to borehole observations. Next, while we focus here on descriptions of the complex behavior that emerges from realistic topographic representations, we suggest initial ways to incorporate complex basal motion into numerical parameterizations applicable to large-scale predictive ice-sheet models. Last, we briefly outline directions for future field studies.

Temperate ice: formation and observations

Large regions of the GrIS's bed, including the majority of its margins, are thawed (*34*). This facilitates fast ice motion through basal-slip but also creates the conditions required for the development of a basal temperate ice layer as we report here. Such a temperate layer has an important but somewhat mysterious role in ice motion as temperate ice is considerably softer than cold ice (*22*, *35*–*38*). This weakness results from liquid water at grain boundaries enhancing diffusion and dislocation creep, dynamic recrystallization, and grain boundary melting [e.g. (*22*, *35*, *39*)] and is particularly important for the basal portions of ice-sheets where the largest deviatoric stresses are focused. Temperate ice can be produced by deformation heating above the CTS, with some studies further suggesting the importance of latent heat transfer across the CTS via water in basal crevasses or ice-grain interfaces (*22*, *30*, *40*, *41*). Conversely, all basal heat sources will reduce temperate layer thickness through basal melt as the positive upwards temperature gradient defined by the Clausius-Clapeyron slope operates as a thermal barrier. Basal heat sources include viscous heat dissipation in flowing subglacial water (*42*), geothermal heat flux, and frictional heat from sliding. While these theoretical underpinnings are well established (*30*, *40*, *43*–*45*), we show that realistic basal topography is the crucial additional component required to explain borehole observations of complex variation in temperate-layer thickness across the GrIS (*19*, *20*, *23*, *28*, *30*, *46*, *47*).

At the Isunnguata Sermia S5 domain, the inter-quartile thickness (obtained across width) of the basal temperate layer increases at 5.6-7.9 m km^{-1} when forced with geostatistically simulated topography. While high variability in the spatial rate of change of temperate layer thickness is to be expected (discussed below), our modelled temperate layer growth rate is compatible with Isunnguata Sermia borehole observations where the temperate layer thickness increases at a rate equivalent to ~4.3 m km^{-1} between site S5 and site S4, located 18.4 km downstream in the direction of flow [Fig. 1B, (*30*)]. As we do not include water transport in our model, our results indicate that roughness-controlled deformation heating alone is sufficient to produce temperate ice at observed rates.

The importance of high-resolution realizations of basal topography is further evident when comparing model outputs forced with geostatistically simulated topography and BedMachine topography, respectively. When topography is smooth (BedMachine run), deformation heat is concentrated within a relatively thin temperate zone and is therefore contributing to internal melt of the temperate layer, not temperate layer growth. A greater basal velocity ratio additionally means basal frictional heating, and therefore basal melt, is increased relative to deformation heat above the CTS. In contrast, perturbations ~200 m across present in geostatistically simulated topography result in ubiquitous spires protruding through the CTS (Fig. 6G-J), which effectively warm cold ice to the point that it becomes temperate. Interestingly, these spires begin to truncate at the CTS as temperate ice thickness increases (Fig. 4C) – which can be explained by the temperate layer now being sufficiently thick as to accommodate a greater proportion of internal deformation – indicating that the temperate layer thickness may not continue to increase linearly indefinitely. This non-linearity, and the situation of S3 on a topographic rise, may explain why the observed increase of the temperate layer at Isunnguata Sermia is smaller than predicted in the S5 model domain in isolation. Overall, we view deformation heating above the CTS as a simpler and more general explanation for temperate layer growth than the hydrological mechanism hypothesized by (*30*, *41*), which requires pervasive basal crevasses or intergranular water transport, both of which lack a clear observational basis.

Localized shear banding and bridges between topographic prominences are further distinctive features of the temperate layer forming in our model. These features are most easily understood by considering their development as the model approaches steady state (fig. S4). As ice slips through a topographic depression it is physically unable to do so without deformation heating increasing the specific enthalpy of the ice locally and downstream and therefore decreasing its

viscosity (Fig. 2A) – a system which stabilizes at the point where deformation heating balances conductive and advective heat losses (*43*). Bridges thereby connect topographic highs where basal-slip is high *sensu stricto* with concentrated internal deformation towards the top of the temperate layer which fills the intervening trough, enabling rapid movement of cold ice over comparatively stagnant temperate ice below. These bridges contribute to some heating above the CTS and occur far more frequently in our two fast-moving domains (RESPONDER and SAFIRE, Figs. 4C, 5A), which may be explained by a velocity threshold controlling the transition between these modes.

Bridges, and (truncated) spires help to explain the complicated temperate ice variation modeled and observed at Sermeq Kujalleq. Spires that protrude through the CTS in the RESPONDER domain (Fig. 4C) increase the temperate layer thickness to a maximum across-flow average of 100 m after 5 km (Fig. 8), beyond which bridges and truncated spires dominate and the rate of temperate layer growth decreases. Convex large-scale ($\gtrsim$2 km) topography further prompts vertical compression and acceleration of the entire ice column, reducing the absolute thickness of the temperate layer and concentrating more deformation below the CTS. This variation is supported by, and further helps to explain, borehole observations of temperate ice. A 73-m-thick temperate layer observed from borehole BH19c (*23*) within the RESPONDER site likely indicates a subglacial topographic depression, while a much smaller temperate-layer thickness (<20 m) only a few kilometers away [but still within the RESPONDER domain, Fig. 1A, (*28*)] is more likely to sample less temperate ice above a topographic prominence. At SAFIRE, dramatic modeled temperate-zone thinning over a notable bedrock rise is compatible with borehole observations from this site showing either a very thin (<8 m) or absent temperate layer (*28*). Here, the convex large-scale topography increases basal-slip and hence reduces internal deformation heating. As with RESPONDER, thinning of the entire ice column over a rise will also locally reduce the absolute thickness of the temperate layer.

Our numerical model also aids interpretation of other GrIS borehole observations. At a site 12.75 km from the ~20 m thick temperate ice layer at S5 (Isunnguata Sermia) and ~1 km south of the main flow line (hereafter IS2015, Fig. 1B), Maier et al. [2019, (*19*)] observe no substantial temperate ice and a high basal-velocity ratio, while a ~100-m-thick layer of temperate ice was observed just 8 km further along flow at sites S4 and S3 (*30*). We suggest that this spatial variability is connected to the topographic rise on which IS2015 was located, which can compress and accelerate the overlying ice in a similar manner to modeled ice motion over the SAFIRE rise beneath Sermeq Kujalleq. However, we also emphasize that stochastic spatial variation in temperate-layer thickness, related to local (100s of m) topographic relief, may play an additional role in inter-site variability. This local variation may further explain observations near Swiss Camp, where temperate layer thickness decreased from ~40 m to ~20 m over 10 km along flow (*20*), which could reflect natural variability as indicated by individual temperate-layer thickness profiles in Fig. 8. Last our findings fully support the existence of an inferred extremely thick (>300 m) basal temperate layer in the deeply eroded basal trough of Sermeq Kujalleq (Jakobshavn Isbræ) formed largely by vertical ice extension (*21*), and offer further avenues to test its importance in fast ice motion. Overall, considerations from our results and from borehole records indicate that large-scale topographic variations (e.g. rises and saddles) control broad patterns of temperate layer thickness, while geostatistically simulated topography is central to the formation of temperate ice and to intermediate-scale ($\geq$25 m, $\lesssim$4 km) variations in its thickness.

These results emphasize the importance of temperate ice, but also the paucity of information regarding temperate ice at micro and macro scales, particularly for the GrIS. Recent laboratory studies on temperate ice are limited [e.g. (*39*, *48*)] and the parameter space for temperate ice flow is relatively unconstrained [e.g. (*22*, *39*, *40*, *49*)], with temperate ice modelling studies mainly directed towards Antarctic shear margins. Although we do not include anisotropy, the rheology of

temperate ice in our model is at the most-viscous end of plausible values (Materials and methods), with less-viscous formulations having the potential to further increase the deformation accommodated within the temperate layer. Alternative drainage formulations for temperate ice may also influence rheological properties and therefore temperate layer behavior (*40*, *50*). While our results reproduce key field observations and provide a framework for understanding temperate ice formation and behavior, further work is urgently required to constrain appropriate parameters and parameterizations for temperate ice.

Complex basal motion: simulations and observations

The model behavior outlined thus far is supported by, and provides an explanation for, the broad spectrum of ice-motion behavior revealed in GrIS borehole records – in addition to the temperate layer thickness variability outlined above. At RESPONDER, damage to a fiber-optic cable at the center of the modeling domain indicated a clear increase in ice deformation towards the top of the temperate ice layer that could not be explained by existing theories (*23*). Our model reproduces this strain behavior when a thicker temperate ice layer occupies a local or broad topographic depression (Fig. 3C, D brown, pink, and blue lines), showing such deformation heterogeneity is an intrinsic part of GrIS ice motion. As this behavior is reproduced with a near-constant rate factor within the modeled temperate layer – a result of uniform water saturation shortly below the CTS – our results further indicate that varying ice rheology is not a prerequisite for variable temperate-layer deformation, as hypothesized in (*23*), but rather, realistic bed topography is. No deformation profile from the BedMachine domain reproduces the fiber-optic cable damage pattern, further indicating that BedMachine topography will not produce realistic ice-motion behavior at intermediate scales ($\lesssim$4 km).

SAFIRE domain model results also show similarly good agreement with observations. Here, Doyle et al. (2018) obtain a basal velocity ratio of 0.63-0.71 and a temperate-layer thickness of up to 8 m, very close to the modal bin of Fig. 7F (sliding ratio 0.75, temperate-layer thickness 4 m). Further, the borehole tilt sensor deformation peak of 1.8 a^{-1} 19 m above the ice sheet base (*28*) is entirely compatible with our modeled deformation rate increases directly (<50 m) above the base (e.g. Fig. 5A, B orange, pink lines). Modeled deformation rates change rapidly with distance above the bed, thus Doyle et al.'s 19-m-above-the-bed sensor may not necessarily represent the maximum rate of deformation within the borehole, which could feasibly continue increasing beyond 1.8 a^{-1} following the gradient between the two lowermost tilt sensors. As our modeling results indicate strain bands are spatially limited yet carry a significant proportion of ice motion, this implies that basal-slip estimates gathered from discrete sensors may be more uncertain and variable than appreciated so far, and – furthermore – be biased towards estimates of greater basal velocity ratio. Another bias comes from the fact that most boreholes in Greenland have been drilled over bedrock highs for practical reasons. Taken together, the SAFIRE and RESPONDER model runs contrast the uniform glacier motion produced in previous Sermeq Kujalleq models forced with smooth BedMachine topography [e.g. (*16*)], and suggest that the complex basal motion is the norm rather than the exception in marine-terminating outlet glacier settings.

Complex basal motion also helps to explain observations from the slower-moving land-terminating ice sheet margin at Isunnguata Sermia that may at first appear contradictory. Site IS2015, just 12.75 km from S5 [Fig. 1B, outlined under Temperate ice formation, (*19*)] has a measured basal velocity ratio ranging from 90.6 to 99.7% and no substantial temperate layer. This basal velocity ratio and temperate layer thickness is distinct from (though not completely incompatible with) the distribution modeled at S5. However, we emphasize that the difference between the closely spaced RESPONDER and SAFIRE domains indicates that a high level of variation forced by different long-wavelength topography is not unusual and should in fact be expected. Our analysis of temperate ice formation along the S5 flowline further suggests that if sliding rates are pervasively as high elsewhere in the Isunnguata Sermia catchment as at IS2015,

then insufficient deformation heat will occur to prompt the very large observed temperate layers at S1-S4 (*30*). Therefore, while it has been hypothesized that sliding is the most important component of ice-motion in land-terminating sectors of the GrIS (*19*), our model shows that sliding dominance is confined to topographic high points and is not a general condition of motion across the GrIS.

Complex basal motion: application to large-scale models

Our process-based understanding of basal motion at small (<25 m) scales has progressed significantly in recent years. Laboratory work for ice overlying deformable sediments (*25*) and 3D numerical-modeling of glacier slip over hard beds with water-filled cavities (*26*) both suggest that basal traction conforms to a regularized-Coulomb relationship: slip resistance first increases with slip velocity before reaching a threshold velocity where till shears at its rate-independent yield strength or cavity dimensions stabilize (Fig. 2B). However, while some large-scale studies support the above experiments [e.g. (*9*, *12*)], this is not universal, with other studies suggesting a Weertman-type slip relationship of ice motion, where basal-traction increases indefinitely with increasing basal velocity (*51*, *52*). The selected basal-slip relationship is then used in an inversion procedure over smooth BedMachine topography for basal-traction parameters that are typically assumed to be time-invariant.

The above contention surrounding appropriate parameterizations has significant ramifications. The choice of basal-slip relationship significantly alters ice-sheet model predictions [e.g. (*10*, *53*–*55*)] and 'deep' process uncertainty in ice-sheet models is a key concern in the most recent IPCC report (*3*). We propose that expanding our conception of ice-sheet motion to include intermediate-scale flow variability ($\geq$25 m, $\lesssim$4 km), and the complexity in topography and basal conditions clearly evident from observations beneath past [e.g. (*56*, *57*)] and present [e.g. (*58*–*61*)] ice sheets, offers a route forward. Parameters derived from inverse methods for heuristically-applied basal-slip relationships (including Weertman or regularized-Coulomb) over smooth BedMachine topography can implicitly account for the complex ice-motion described here. However, while parameters from inversions may reproduce observed velocities well, divergence between predicted and actual ice-sheet behavior is likely to increase over model time if the *form* of the basal-motion relationship is an incorrect representation of intermediate-scale basal motion processes and does not account for temporal changes in motion conditions (*62*), such as a local change in temperate layer thickness influencing the basal velocity ratio.

Incorporating the process-based understanding we have generated here into a parameterization that explicitly accounts for basal-motion over realistic topography, in addition to basal-slip, provides a potential solution. This is achievable by treating basal temperate ice as a distinct layer that includes both internal deformation and basal-slip. This approach would yield a high CTS velocity ratio akin to the one produced for basal slip using BedMachine topography. Application of geostatistically generated topography to BedMachine in full ice-sheet models is not a requirement. If the developed basal-motion relationship can account for spatial variations in geostatistical parameters, then coarse-resolution grid cells can still be effectively used, with the knowledge that complex basal topography and processes are still parametrically incorporated. Further geological considerations are outlined in the supplementary text. Development and implementation of such a basal-motion relationship will increase confidence that predictive ice-sheet models are accurately representing the complex reality of ice-sheet motion and may therefore improve the accuracy of sea-level rise predictions.

Outlook

Our results show that while the basal velocity ratio and temperate layer thickness can vary across a small region (~0.25 km^2) and may mimic catchment-scale results, most small regions in isolation will not be representative of basal-motion at larger scales. A focus in field studies on

coarser (≳1 km) borehole arrays covering a wider range of topographic features may therefore enable more accurate characterization of ice-motion variability. Separately, as temperate layer thickness variation is directly influenced by deformation heating within the ice and hence the basal velocity ratio, intensive borehole- and radar-based investigation across a domain similar in size to the ones used here would allow improved estimates of parameters by fitting model data to observations.

Overall, our results indicate unavoidable complexity in descriptions of ice-sheet motion. We provide a unified explanation for borehole observations of spatial variability in basal temperate ice thickness and basal velocity ratio, and for down-borehole variability in deformation rates. In sum, we hope that these advances in understanding will facilitate the development of improved representations of ice-sheet motion and hence more accurate predictions of sea level rise.

Materials and methods

Numerical modelling

We model ice flow in rectangular 8 km (along flow) by 4 km (across flow) domains oriented along flow where the x y z axes define length, width, and depth, respectively (Fig. 1f). This allows a high mesh resolution and a focus on basal-motion processes, without requiring modeling of an entire glacier catchment. To obtain realistic boundary conditions for our model domains we first use time-evolving runs with periodic inflow-outflow conditions and a free surface (FS runs) to determine the gravity vector orientation (or slope) needed to approximate satellite-derived glacier velocities characterizing each domain. We then obtain a free-surface DEM, surface pressure field, and inflow boundary conditions for the velocity vector components and pressure. We use these derived boundary conditions and gravity-vector orientation on the same domain for the final thermomechanically coupled runs (TC runs) in which the enthalpy and velocity fields are allowed to evolve until steady-state convergence is reached. TC runs are not compatible with periodic domains as it is unphysical for the enthalpy field and hence rheological characteristics at the outflow boundary to match the inflow boundary.

We use the Elmer/Ice (version 9.0) finite element modeling package (*63*) on GNU/Linux with 191.9 GB total memory and 18 @2.20 GHz processor partitions for all runs. FS runs take ~5 days, TC runs take ~12 hr. A triangular mesh with representative edge length of 25 m and ~124,119 triangular elements is made with Gmsh and vertically extruded using the Elmer/Ice StructuredMeshMapper, with vertical layer spacing decreasing towards the base. Further increasing the spatial resolution does not meaningfully alter model output (fig. S5). FS runs use 25 vertical layers to reduce computation time, increased to 42 for TC runs, giving a lowermost cell thickness of 1.6 m for an ice column of 1 km (Fig. S6). Domains are centered about a borehole location, with the basal topography normalized such that the average DEM value is equivalent to the negative of the thickness obtained by the central borehole(s), giving an initially flat surface with z coordinate 0 m. To maintain inflow outflow boundaries at the same z coordinates, the SAFIRE domain is additionally detrended to remove an average slope of 2.7°. Table 1 provides details on specific run setups. Table S2 provides parameter and constant values.

We solve the standard Stokes equations governing ice flow,

$\nabla \cdot \boldsymbol{u} = 0$ (conservation of mass), (1)
$\nabla \cdot \boldsymbol{\tau} - \nabla \cdot p = -\rho \boldsymbol{g}$ (balance of momentum), (2)

where $\boldsymbol{u} = u_i$ (m a^{-1}) is the ice velocity, $\boldsymbol{\tau} = \tau_{ij}$ (MPa) is the deviatoric stress tensor, p (MPa) is the ice pressure, ρ (MPa m^{-2} a^{-2}) is the ice density (assumed constant, with no adjustment for water content) and $\boldsymbol{g} = g_i$ (m a^{-2}) is the gravitational acceleration vector. The slope, θ (°), is set

by assigning $\boldsymbol{g} = [gsin(\theta), 0, -gcos(\theta)\,]$, where $g = 9.81$ m a^{-2}, to remove the requirement for vertical displacement of periodic inflow-outflow boundaries. Stress is related to strain using the Nye-Glen isotropic flow law (*64*, *65*),

$$\dot{\boldsymbol{\epsilon}} = A\tau_e^{n-1}\boldsymbol{\tau} \tag{3}$$

where $\dot{\boldsymbol{\epsilon}} = \dot{\epsilon}_{ij} = \frac{1}{2}\left(\frac{\partial u_i}{\partial x_j} + \frac{\partial u_j}{\partial x_i}\right)$ (a^{-1}) is the strain rate tensor, $\tau_e^2 = \frac{1}{2}tr(\tau^2)$ (MPa) is the effective stress in the ice, n is the flow exponent assumed to equal 3, and A is the creep parameter (MPa^{-3} a^{-1}). A is calculated from the homologous temperature, T_h (K), if below the pressure-dependent melting point, T_m, or water content, ω (proportion), if above as

$$A = \begin{cases} A_1 exp\left(\frac{Q_1}{RT_h}\right), & T_h \le T_{lim} \\ A_2 exp\left(\frac{Q_2}{RT_h}\right), & T_{lim} < T_h < T_m \\ (W_1 + W_2\omega \times 100)W_3, & T_h \ge T_m, \;\; \omega < \omega_{llm} \\ A_{max}, & \omega \ge \omega_{lim} \end{cases} \tag{4}$$

where $T_m(p) = T_{tr} - \gamma(p - p_{tr})$ where γ (K MPa^{-1}) is the Clausius-Clapeyron constant, T_{tr} is the triple point water temperature, and p_{tr} is the triple point water pressure. A_1 and A_2 are rate factors (MPa a^{-1}) and Q_1 and Q_2 are activation energies (J mol^{-1}) for $T \le T_{lim}$ and $T_{lim} < T < T_m$ respectively where $T_{lim} = 263.2$ K is the limit temperature. R is the gas constant (J mol^{-1} K^{-1}) and W_1, W_2, and W_3 (all in MPa a^{-1}) are water viscosity factors, with default values taken from the linear fit of Duval [1977, (*35*)] adapted by Haseloff et al. [2019, (*49*)] for water contents up to 0.7±0.1% under tertiary creep. We hold W_1, W_2, and W_3 constant for all model runs and set a conservative limit for ω_{lim} of 0.6% as Adams et al. [2021, (*39*)] propose A does not increase between water contents of 0.6-2% following experiments conducted under secondary creep. Once ω_{lim} is exceeded $A = A_{max}$, limiting the rate factor of temperate ice. Fig. 2a shows the increase of A with temperature and then water content as used in our model.

Specific enthalpy, H (J kg^{-1}), is used as the state variable with the Elmer/Ice EnthalpySolver (*66*) and is related to T and ω as

$$H(T, \omega) = \begin{cases} \frac{1}{2}C_a\left(T^2 - {T_{ref}}^2\right) + C_b\left(T - T_{ref}\right), & H < H_m(p) \\ \omega L + H_m, & H \ge H_m(p) \end{cases} \tag{5}$$

where C_a (J kg^{-1} K^{-2}) and C_b (J kg^{-1} K^{-1}) are enthalpy heat capacity constants, L (J kg^{-1}), is the latent heat capacity of ice, $H_m(p) = \frac{1}{2}C_a\left(T_m(p)^2 - {T_{ref}}^2\right) + C_b\left(T_m(p) - T_{ref}\right)$ is the specific enthalpy at the pressure-dependent melting point, and T_{ref} = 200 K is the reference temperature.

Our mesh representative edge length of 25 m makes the use of a physically-derived small-scale sliding relationship most appropriate and so we follow the regularized-Coulomb relationship of (*30*) and (*29*). Basal traction, τ_b (MPa), is given as

$$\tau_b = CN_e\left(\frac{{u_b}^{-n+1}}{u_b + A_s C^n N_e^n}\right)^{\frac{1}{n}} u_b \tag{6}$$

where C (dimensionless) is a parameter that depends on basal morphology and cannot be readily estimated from irregular topographies but must be less than the maximum up-slope gradient of the bed (*26*), u_b, is the basal velocity (m a^{-1}) tangential to the ice-bed interface, $n = 3$ is the same exponent used in the flow relationship. A_s (m a^{-1} MPa^{-3}) depends on ice rheology and morphology of the bed and is used in the case of hard-bed sliding with no cavitation (*67*), and N_e (MPa) is the effective pressure at the bed. (*26*) provide six values for A_s and C based on representative element-area DEMs obtained from un-crewed aerial-vehicle surveys on bedrock surfaces recently exposed by glacier recession. We take the average of these six values for each of A_s and C as constant for all runs rather than apply a basal-traction inversion procedure that would require inherent assumptions about ice deformation. N_e is then varied as the only free parameter controlling basal traction though we note this has a similar effect to varying C.

We make the simplifying assumption that N_e is related to the overburden pressure alone via a proportionality parameter, O (dimensionless), as $N_e = -\rho g_z O(s - b)$ where b (m) is the elevation of the glacier base and s (m) is the surface elevation. However, basal traction has an upper limit under Eq. 6 of $\tau_{b_{max}} = N_e C$ which can lead to instability when the average driving stress, $\tau_d = \rho g h sin(\theta)$, cannot be supported within the modeling domain, leading to the inequality

$$O \leq \frac{F\, sin(\theta)}{C} \qquad (7)$$

where F is a parameter that would equal 1 if $\tau_{b_{max}} \approx \tau_d$. In practice, the model ceases to converge to reasonable values for RESPONDER BedMachine runs if $F \lesssim 1.15$ and for RESPONDER geostatistical runs if $F \lesssim 0.85$ due to the additional support from the stoss side of basal obstacles. To ensure we are sufficiently within the convergence space of the system we set $F = 1.2$ for all BedMachine runs, and run geostatistical runs with $F = 1.2$ and $F = 0.9$. We note that we are therefore close to maximum possible sliding rates given our domain geometries where force balance is met locally (which is similar to the assumptions of the shallow-ice approximation). Fig. 2B illustrates the range of behavior for τ_b with $F = 1.2$ and $s - b = 1{,}043$ m. For the range of slopes and F values covered and $C = 0.1617$, this gives a range in O from 0.0.0874 to 0.240, comparable to values in other studies (*42*, *68*). Increasing the proportion of driving stress supported by the maximum basal traction value slightly shifts the basal-velocity-ratio distribution towards lower values, with a new mode of 0.28 (fig. S3). θ is then altered in 0.05° increments (with concomitant change in O) to obtain the best match between modeled surface velocity and satellite measurements. Surface slopes in the regions studied are 1-2° with variation in $\boldsymbol{g}$ away from the long-wavelength borehole site value expected as $\boldsymbol{g}$ in our model will also be accounting for longitudinal and transverse stresses in the ice.

Free-surface runs

In FS runs enthalpy and hence A is calculated as a function of normalized depth, $D = \frac{d}{b+s}$, where d (m) is depth, as $H = E_a D^2 + E_b D + E_c$ where E_a, E_b, and E_c are quadratic curve parameters. E_a, E_b, and E_c are obtained via a second-order polynomial fitting procedure (Matlab polyfit) of borehole data with minor adjustments to only just remove the temperate ice layer (Fig. S7). This approach ensures consistent rheology at the periodic inflow-outflow boundaries. These profiles are also used for the input enthalpy field in TC runs.

The free surface is computed with the Elmer/Ice FreeSurfaceSolver as

$$\frac{\partial s}{\partial t} + u_x \frac{\partial s}{\partial x} + u_y \frac{\partial s}{\partial y} = u_z \quad (9)$$

where u_x, u_y, u_z are components of the surface velocity vector $\boldsymbol{u}$. No accumulation or ablation is accounted for as this would require a corresponding removal of mass from elsewhere in the model hence u_z = 0. The timestep is set to 0.015 a and the simulation is stopped when the maximum and minimum surface show only minor variation (Fig. S8). The free surface DEM, surface pressure field, and inflow pressure and velocity fields are then extracted and reprojected as boundary conditions onto the TC mesh.

Thermomechanically coupled runs

The specific enthalpy field is allowed to freely evolve until a steady-state is reached and is calculated as

$$\rho\left(\frac{\partial H}{\partial t} + \boldsymbol{u} \cdot \nabla H\right) = \nabla(\kappa \nabla H) + tr(\boldsymbol{\tau}\dot{\boldsymbol{\epsilon}}) \quad (10)$$

where $tr(\boldsymbol{\tau}\dot{\boldsymbol{\epsilon}})$ is the strain heating term. κ (kg m^{-1} s^{-1}) is the enthalpy diffusivity defined as

$$\kappa = \begin{cases} \kappa_c, & H < H_m(p) \\ \kappa_t, & H \geq H_m(p) \end{cases} . \quad (11)$$

where κ_c and κ_t are enthalpy diffusivities for cold and temperate ice respectively, meaning water movement within the temperate ice is assumed to be a diffusive process. H is limited by ω_{max} set at 2.5%, around the level of field observations of water content ((*69*) and references therein). However, as we limit increases in A to water contents of 0.6% we note that a greater maximum water content value only acts to increase water-content gradient and hence enthalpy transfers within the temperate zone and across the cold-temperate transition zone, though κ_t is an order of magnitude lower than κ_c.

Drainage is treated simply by setting an upper specific enthalpy limit equivalent to ω_{max} with drainage assumed to occur instantaneously above this threshold. Vertically integrated drainage volumes, D_v (m^3 a^{-1}), are then obtained from specific enthalpy loads, H_{loads}, and element weighting, $H_{weights}$, as

$$D_v = \int_b^{CTS} \frac{H_{loads}}{H_{weights}} dz \quad (12)$$

where CTS is the z coordinate of the cold-temperate transition surface. More advanced drainage formulations exist (*40*, *50*) but their implementation is beyond the scope of this paper.

For the purposes of basal sliding, we make no adjustment for the small sections where basal temperatures are below the pressure melting point, effectively assuming that the bed is sufficiently-well hydrologically connected to provide water to these regions for freeze-on. Considerations for basal freeze-on rates required to pin the basal temperature at the pressure melting point are presented in the Supplementary material, showing the water required is negligible in context. The basal mass balance, M_b (kg m^{-2} a^{-1}), is calculated as

$$M_b = \frac{1}{H}(F_b + Q_b + \boldsymbol{G}_b \cdot \boldsymbol{n}_b - \boldsymbol{q} \cdot \boldsymbol{n}_b) \quad (13)$$

where $F_b = u_b \tau_b$ is the frictional heating at the bed, $\boldsymbol{G}_b$ is the geothermal heat flux, $\boldsymbol{n}_b$ is the basal normal vector, $\boldsymbol{q} = -k\nabla T$ is the energy flux into the ice where k is the thermal conductivity of the ice, and Q_b is the rate at which hydrological storage and transport mechanisms deliver latent heat to the base of the ice which we set as 0 across all of our model domains. When a temperate layer is present $\boldsymbol{q}$ is a small negative value (flux directed towards the base) determined by the local pressure gradient. If no temperate layer is present $\boldsymbol{q}$ is a small positive value (directed away from the base). Comparisons of inflowing and outflowing ice volumes for the RESPONDER BedMachine run, where mass loss is greatest, shows basal melting has a negligible effect on overall ice flow volumes (0.3%). Elmer/Ice solver input files and post-processing scripts are available in the Supplementary material.

Geostatistical DEM simulations

We use conditional geostatistical simulations (*70*) to produce DEMs for each site that (a) match basal topography from radar flight lines that cross each domain, (b) reproduce the roughness exhibited in radar flight line profiles (Fig. 1), and (c) retain the long-wavelength (≳2 km) features of BedMachine. In order to create the most direct comparison with BedMachine topography (*14*) we simulate topography by adding roughness to BedMachine based on the characteristics of the residual between BedMachine and radar measurements. It is customary to simulate multiple realizations in order to quantify uncertainty [e.g. (*33*)]; however, no great variation in the form of the hexbin cloud for the RESPONDER domain is produced when the model is forced with topography from the second topographic realizations of this region (Fig. S3, Materials and methods), so only one realization is used for the SAFIRE and S5 domains. Two realizations are used for the RESPONDER domain for a sensitivity analysis.

The simulation is carried out in the following steps. First, the residuals between BedMachine v3 and CReSIS radar measurements [from 1993 to 2017, (*29*)] are calculated. We included all data within a 5 km buffer around each study area so that these observations can serve as outside constraints on the simulations. Residual data is used rather than raw radar measurements to ensure the simulated topography retains long-wavelength BedMachine features. A normal score transformation is then performed on the residuals so that the data conforms to standard Gaussian assumptions required by the simulation algorithm. An empirical variogram $\hat{\gamma}(h)$, is produced for each site to quantify spatial covariance, or topographic roughness (Fig. 1C, D). The variogram relates the variance of each pair of residual bed measurements to their separation (lag) distance. The variance increases with lag distance. For example, two bed measurements that are close together typically have a low variance because nearby points often have similar values. However, at large lag distances, the variance is much greater because bed measurements that are far apart are not strongly correlated. The empirical variogram is calculated as

$$\hat{\Gamma}(h) = \frac{1}{2N(h)} \sum_{\alpha=1}^{N} (b(x_\alpha) - b(x_\alpha + h))^2 \quad (14)$$

where $b(x_\alpha)$ is measured bed topography, x_α is a spatial location, and N is the number of point pairs for a given lag distance, h (m). Each empirical variogram was calculated with different azimuthal directions in order to capture any roughness anisotropy. A variogram model is manually fitted to the empirical variogram. For S5 the modeled variogram is

$$\Gamma(h) = 0.4 + 0.6 * exp(h, 1600) \quad (15)$$

where $exp\ (h, c)$ is the exponential variogram function with a range c (m) (*70*). The S5 model variogram has a nugget of 0.4 which represents the short-range variability. No significant topographic anisotropy was found. The RESPONDER model variogram is fitted as

$$\Gamma(h) = 0.1 + 0.9 * sph(h, 2100) \quad (16)$$

where $sph(h, a)$ is the spherical variogram function (*71*). The RESPONDER model variogram has a smaller nugget and larger range than the S5 model variogram, indicating smoother residual roughness at RESPONDER. The RESPONDER model variogram is also isotropic.

The modeled variograms are then used to perform a sequential Gaussian simulation which produces random realizations of phenomena such that the output realization has the same spatial covariance as the input data [e.g. (*70*)]. The sequential Gaussian simulation uses a random path to visit each grid cell and simulate a value. At each grid cell, the variogram is used to estimate the mean and variance of bed, which defines a Gaussian probability distribution. While kriging interpolation will select the mean of the distribution, sequential Gaussian simulation randomly draws from the distribution to generate a simulated value. To ensure a seamless interpolation, each simulated value is constrained by previously simulated grid cells. This process is repeated until every grid cell is populated. This technique has previously been used to simulate the basal topography of Sermeq Kujalleq (also known as Jakobshavn Isbræ) in west Greenland (*33*).

The simulated residual roughness is then back-transformed to recover the original data distribution and added to BedMachine data to produce output DEMs. A Gaussian filter with standard deviation 1.5 is applied to remove very short wavelength ($\lesssim$50 m) topographic features which can cause unrealistic model behavior. The simulation was implemented using the GeostatsPy software package (*72*). For a detailed description of the methodology, see (*70*) and (*73*) and workflow scripts in the Supplementary material. Last, a tapering algorithm detailed in (*26*) is applied to the final 1.6 km of the DEMs to ensure periodic boundaries have equal elevations and minimize topographic modification.

References

1. J. Mouginot, E. Rignot, A. A. Bjørk, M. van den Broeke, R. Millan, M. Morlighem, B. Noël, B. Scheuchl, M. Wood, Forty-six years of Greenland Ice Sheet mass balance from 1972 to 2018. *Proc. Natl. Acad. Sci. U. S. A.* **116**, 9239–9244 (2019).
2. A. Aschwanden, T. C. Bartholomaus, D. J. Brinkerhoff, M. Truffer, Brief communication: A roadmap towards credible projections of ice sheet contribution to sea level. *Cryosphere*. **15**, 5705–5715 (2021).
3. V. MassonDelmotte, P. Zhai, A. Pirani, S. L. Connors, C. Péan, S. Berger, N. Caud, Y. Chen, L. Goldfarb, M. I. Gomis, M. Huang, K. Leitzell, E. Lonnoy, J. B. R. Matthews, T. K. Maycock, T. Waterfield, O. Yelekçi, R. Yu, B. Zhou, "Summary for Policymakers. In: Climate Change 2021: The Physical Science Basis. Contribution of Working Group I to the Sixth Assessment Report of the Intergovernmental Panel on Climate Change" (2021), , doi:10.1017/9781009157896.001.
4. H. Goelzer, S. Nowicki, A. Payne, E. Larour, H. Seroussi, W. H. Lipscomb, J. Gregory, A. Abe-Ouchi, A. Shepherd, E. Simon, C. Agosta, P. Alexander, A. Aschwanden, A. Barthel, R. Calov, C. Chambers, Y. Choi, J. Cuzzone, C. Dumas, T. Edwards, D. Felikson, X. Fettweis, N. R. Golledge, R. Greve, A. Humbert, P. Huybrechts, S. Le Clec'H, V. Lee, G. Leguy, C. Little, D. Lowry, M. Morlighem, I. Nias, A. Quiquet, M. Rückamp, N. J. Schlegel, D. A. Slater, R. Smith, F. Straneo, L. Tarasov, R. Van De Wal, M. Van Den

Broeke, The future sea-level contribution of the Greenland ice sheet: A multi-model ensemble study of ISMIP6. *Cryosphere.* **14**, 3071–3096 (2020).
5. A. Aschwanden, M. A. Fahnestock, M. Truffer, D. J. Brinkerhoff, R. Hock, C. Khroulev, R. Mottram, S. Abbas Khan, Contribution of the Greenland Ice Sheet to sea level over the next millennium. *Sci. Adv.* **5**, eaav9396 (2019).
6. S. Hofer, C. Lang, C. Amory, C. Kittel, A. Delhasse, A. Tedstone, X. Fettweis, Greater Greenland Ice Sheet contribution to global sea level rise in CMIP6. *Nat. Commun.* **11**, 6289 (2020).
7. Y. Choi, M. Morlighem, E. Rignot, M. Wood, Ice dynamics will remain a primary driver of Greenland ice sheet mass loss over the next century. *Commun. Earth Environ.* **2**, 26 (2021).
8. P. D. Bons, T. Kleiner, M.-G. Llorens, D. J. Prior, T. Sachau, I. Weikusat, D. Jansen, Greenland Ice Sheet: Higher Nonlinearity of Ice Flow Significantly Reduces Estimated Basal Motion. *Geophys. Res. Lett.* **45**, 6542–6548 (2018).
9. I. Joughin, B. E. Smith, C. G. Schoof, Regularized Coulomb Friction Laws for Ice Sheet Sliding: Application to Pine Island Glacier, Antarctica. *Geophys. Res. Lett.* **46**, 4764–4771 (2019).
10. J. Brondex, F. Gillet-Chaulet, O. Gagliardini, Sensitivity of centennial mass loss projections of the Amundsen basin to the friction law. *Cryosphere*. **13**, 177–195 (2019).
11. G. Durand, O. Gagliardini, L. Favier, T. Zwinger, E. Le Meur, Impact of bedrock description on modeling ice sheet dynamics. *Geophys. Res. Lett.* **38**, L20501 (2011).
12. V. C. Tsai, A. L. Stewart, A. F. Thompson, Marine ice-sheet profiles and stability under Coulomb basal conditions. *J. Glaciol.* **61**, 205–215 (2015).
13. M. R. Van Den Broeke, E. M. Enderlin, I. M. Howat, P. K. Munneke, B. P. Y. Noël, W. J. Van De Berg, E. Van Meijgaard, B. Wouters, On the recent contribution of the Greenland ice sheet to sea level change. *Cryosph.* **10**, 1933–1946 (2016).
14. M. Morlighem, C. N. Williams, E. Rignot, L. An, J. E. Arndt, J. L. Bamber, G. Catania, N. Chauché, J. A. Dowdeswell, B. Dorschel, I. Fenty, K. Hogan, I. Howat, A. Hubbard, M. Jakobsson, T. M. Jordan, K. K. Kjeldsen, R. Millan, L. Mayer, J. Mouginot, B. P. Y. Noël, C. O'Cofaigh, S. Palmer, S. Rysgaard, H. Seroussi, M. J. Siegert, P. Slabon, F. Straneo, M. R. van den Broeke, W. Weinrebe, M. Wood, K. B. Zinglersen, BedMachine v3: Complete Bed Topography and Ocean Bathymetry Mapping of Greenland From Multibeam Echo Sounding Combined With Mass Conservation. *Geophys. Res. Lett.* **44**, 11051–11061 (2017).
15. E. J. MacKie, D. M. Schroeder, Geostatistically Simulating Subglacial Topography with Synthetic Training Data. *Int. Geosci. Remote Sens. Symp.*, 2991–2994 (2020).
16. S. J. Cook, P. Christoffersen, J. Todd, D. Slater, N. Chauché, Coupled modelling of subglacial hydrology and calving-front melting at Store Glacier, West Greenland. *Cryosphere*. **14**, 905–924 (2020).
17. A. Aschwanden, M. A. Fahnestock, M. Truffer, Complex Greenland outlet glacier flow captured. *Nat. Commun.* **7**, 10524 (2016).
18. T. J. Young, P. Christoffersen, S. H. Doyle, K. W. Nicholls, C. L. Stewart, B. Hubbard, A. Hubbard, L. B. Lok, P. V. Brennan, D. I. Benn, A. Luckman, M. Bougamont, Physical Conditions of Fast Glacier Flow: 3. Seasonally-Evolving Ice Deformation on Store Glacier, West Greenland. *J. Geophys. Res. Earth Surf.* **124**, 245–267 (2019).
19. N. Maier, N. Humphrey, J. Harper, T. Meierbachtol, Sliding dominates slow-flowing margin regions, Greenland Ice Sheet. *Sci. Adv.* **5**, eaaw5406 (2019).
20. C. Ryser, M. P. Lüthi, L. C. Andrews, M. J. Hoffman, G. A. Catania, R. L. Hawley, T. A. Neumann, S. S. Kristensen, Sustained high basal motion of the Greenland ice sheet revealed by borehole deformation. *J. Glaciol.* **60**, 647–660 (2014).
21. Lüthi, M. Funk, A. Iken, S. Gogineni, M. Truffer, Mechanisms of fast flow in Jakobshavn

Isbræ, West Greenland: Part III. Measurements of ice deformation, temperature and cross-borehole conductivity in boreholes to the bedrock. *J. Glaciol.* **48**, 369–385 (2002).
22. M. Krabbendam, Sliding of temperate basal ice on a rough, hard bed: creep mechanisms, pressure melting, and implications for ice streaming. *Cryosph.* **10**, 1915–1932 (2016).
23. R. Law, P. Christoffersen, B. Hubbard, S. H. Doyle, T. R. Chudley, C. Schoonman, M. Bougamont, B. des Tombe, B. Schilperoort, C. Kechavarzi, A. Booth, T. J. Young, Thermodynamics of a fast-moving Greenlandic outlet glacier revealed by fiber-optic distributed temperature sensing. *Sci. Adv.* **7**, eabe7136 (2021).
24. C. Ryser, M. P. Lüthi, L. C. Andrews, G. A. Catania, M. Funk, R. Hawley, M. Hoffman, T. A. Neumann, Caterpillar-like ice motion in the ablation zone of the Greenland ice sheet. *J. Geophys. Res. Earth Surf.* **119**, 2258–2271 (2014).
25. L. K. Zoet, N. R. Iverson, A slip law for glaciers on deformable beds. *Science (80-.).* **368**, 76–78 (2020).
26. C. Helanow, N. R. Iverson, J. B. Woodard, L. K. Zoet, A slip law for hard-bedded glaciers derived from observed bed topography. *Sci. Adv.* **7**, eabe7798 (2021).
27. A. L. Hubbard, B. Hubbard, P. Christoffersen, S. H. Doyle, T. R. Chudley, C. M. Schoonman, R. Law, M. Bougamont, *AGU Adv.*, in press, doi:10.1029/2020AV000291.
28. S. H. Doyle, B. Hubbard, P. Christoffersen, T. J. Young, C. Hofstede, M. Bougamont, J. E. Box, A. Hubbard, Physical Conditions of Fast Glacier Flow: 1. Measurements From Boreholes Drilled to the Bed of Store Glacier, West Greenland. *J. Geophys. Res. Earth Surf.* **123**, 324–348 (2018).
29. CReSIS, CReSIS radar depth sounder data. *Cent. Remote Sens. Ice Sheets, Lawrence, Kansas, USA. Digit. Media* (2021), (available at https://data.cresis.ku.edu/).
30. J. A. Harrington, N. F. Humphrey, J. T. Harper, Temperature distribution and thermal anomalies along a flowline of the Greenland ice sheet. *Ann. Glaciol.* **56**, 98–104 (2015).
31. K. M. Cuffey, W. S. B. Paterson, *The Physics of Glaciers* (Elsevier Science & Technology Books, Amsterdam, ed. 4, 2010).
32. M. Morlighem, E. Rignot, H. Seroussi, E. Larour, H. Ben Dhia, D. Aubry, A mass conservation approach for mapping glacier ice thickness. *Geophys. Res. Lett.* **38**, L19503 (2011).
33. E. J. MacKie, D. M. Schroeder, C. Zuo, Z. Yin, J. Caers, Stochastic modeling of subglacial topography exposes uncertainty in water routing at Jakobshavn Glacier. *J. Glaciol.* **67**, 75–83 (2021).
34. J. A. MacGregor, M. A. Fahnestock, G. A. Catania, A. Aschwanden, G. D. Clow, W. T. Colgan, S. P. Gogineni, M. Morlighem, S. M. J. Nowicki, J. D. Paden, S. F. Price, H. Seroussi, A synthesis of the basal thermal state of the Greenland Ice Sheet. *J. Geophys. Res. Earth Surf.* **121**, 1328–1350 (2016).
35. P. Duval, The role of the water content on the creep rate of poly-crystalline ice. *Int. Assoc. Hydrol. Sci. Publ.* **118**, 29–33 (1977).
36. L. Lliboutry, Physical Processes in Temperate Glaciers. *J. Glaciol.* **16**, 151–158 (1976).
37. V. I. Morgan, High-temperature ice creep tests. *Cold Reg. Sci. Technol.* **19**, 295–300 (1991).
38. S. C. Colbeck, R. J. Evans, A Flow Law for Temperate Glacier Ice. *J. Glaciol.* **12**, 71–86 (1973).
39. C. J. C. Adams, N. R. Iverson, C. Helanow, L. K. Zoet, C. E. Bate, Softening of Temperate Ice by Interstitial Water. *Front. Earth Sci.* **9**, 702761 (2021).
40. I. J. Hewitt, C. Schoof, Models for polythermal ice sheets and glaciers. *Cryosph.* **11**, 541–551 (2017).
41. J. T. Harper, J. H. Bradford, N. F. Humphrey, T. W. Meierbachtol, Vertical extension of the subglacial drainage system into basal crevasses. *Nature*. **467**, 579–582 (2010).

42. K. D. Mankoff, S. M. Tulaczyk, The past, present, and future viscous heat dissipation available for Greenland subglacial conduit formation. *Cryosph.* **11**, 303–317 (2017).
43. A. Aschwanden, E. Bueler, C. Khroulev, H. Blatter, An enthalpy formulation for glaciers and ice sheets. *J. Glaciol.* **58**, 441–457 (2012).
44. R. Greve, H. Blatter, *Dynamics of Ice Sheets and Glaciers* (Springer, Berlin, 2009).
45. Y. Wang, T. Zhang, C. Xiao, J. Ren, Y. Wang, A two-dimensional, higher-order, enthalpy-based thermomechanical ice flow model for mountain glaciers and its benchmark experiments. *Comput. Geosci.* **141**, 104526 (2020).
46. J. Seguinot, M. Funk, A. Bauder, T. Wyder, C. Senn, S. Sugiyama, Englacial Warming Indicates Deep Crevassing in Bowdoin Glacier, Greenland. *Front. Earth Sci.* **8**, 65 (2020).
47. A. Iken, K. Echelmeyer, W. Harrison, M. Funk, Mechanisms of fast flow in Jakobshavns Isbræ, West Greenland: Part I. Measurements of temperature and water level in deep boreholes. *J. Glaciol.* **39**, 15–25 (1993).
48. J. R. Fowler, N. R. Iverson, A permeameter for temperate ice: first results on permeability sensitivity to grain size. *J. Glaciol.*, 1–11 (2022).
49. M. Haseloff, I. J. Hewitt, R. F. Katz, Englacial Pore Water Localizes Shear in Temperate Ice Stream Margins. *J. Geophys. Res. Earth Surf.* **124**, 2521–2541 (2019).
50. C. Schoof, I. J. Hewitt, A model for polythermal ice incorporating gravity-driven moisture transport. *J. Fluid Mech.* **797**, 504–535 (2016).
51. N. Maier, F. Gimbert, F. Gillet-Chaulet, A. Gilbert, Basal traction mainly dictated by hard-bed physics over grounded regions of Greenland. *Cryosphere*. **15**, 1435–1451 (2021).
52. F. Gimbert, A. Gilbert, O. Gagliardini, C. Vincent, L. Moreau, *Geophys. Res. Lett.*, in press, doi:10.1029/2021GL092858.
53. T. M. Kyrke-Smith, G. H. Gudmundsson, P. E. Farrell, Relevance of detail in basal topography for basal slipperiness inversions: A case study on Pine Island Glacier, Antarctica. *Front. Earth Sci.* **11**, 33 (2018).
54. F. Gillet-Chaulet, G. Durand, O. Gagliardini, C. Mosbeux, J. Mouginot, F. Rémy, C. Ritz, *Geophys. Res. Lett.*, in press, doi:10.1002/2016GL069937.
55. B. R. Parizek, K. Christianson, S. Anandakrishnan, R. B. Alley, R. T. Walker, R. A. Edwards, D. S. Wolfe, G. T. Bertini, S. K. Rinehart, R. A. Bindschadler, S. M. J. Nowicki, Dynamic (in)stability of Thwaites Glacier, West Antarctica. *J. Geophys. Res. Earth Surf.* **118**, 638–655 (2013).
56. M. Krabbendam, N. Eyles, N. Putkinen, T. Bradwell, L. Arbelaez-Moreno, Streamlined hard beds formed by palaeo-ice streams: A review. *Sediment. Geol.* **338**, 24–50 (2016).
57. D. H. Roberts, A. J. Long, Streamlined bedrock terrain and fast ice flow, Jakobshavns Isbrae, West Greenland : implications for ice stream and ice sheet dynamics. *Boreas*. **34**, 25–42 (2005).
58. N. Holschuh, K. Christianson, J. Paden, R. B. Alley, S. Anandakrishnan, Linking postglacial landscapes to glacier dynamics using swath radar at Thwaites Glacier, Antarctica. *Geology*. **48**, 268–272 (2020).
59. R. G. Bingham, D. G. Vaughan, E. C. King, D. Davies, S. L. Cornford, A. M. Smith, R. J. Arthern, A. M. Brisbourne, J. De Rydt, A. G. C. Graham, M. Spagnolo, O. J. Marsh, D. E. Shean, Diverse landscapes beneath Pine Island Glacier influence ice flow. *Nat. Commun.* **8**, 1618 (2017).
60. C. F. Dow, A. Hubbard, A. D. Booth, S. H. Doyle, A. Gusmeroli, B. Kulessa, Seismic evidence of mechanically weak sediments underlying Russell Glacier, West Greenland. *Ann. Glaciol.* **54**, 135–141 (2013).
61. J. T. Harper, N. F. Humphrey, T. W. Meierbachtol, J. A. Graly, U. H. Fischer, Borehole measurements indicate hard bed conditions, Kangerlussuaq sector, western Greenland Ice Sheet. *J. Geophys. Res. Earth Surf.* **122**, 1605–1618 (2017).

62. H. Goelzer, A. Robinson, H. Seroussi, R. S. W. van de Wal, Recent Progress in Greenland Ice Sheet Modelling. *Curr. Clim. Chang. Reports*. **3**, 291–302 (2017).
63. O. Gagliardini, T. Zwinger, F. Gillet-Chaulet, G. Durand, L. Favier, B. De Fleurian, R. Greve, M. Malinen, C. Martín, P. Räback, J. Ruokolainen, M. Sacchettini, M. Schäfer, H. Seddik, J. Thies, Capabilities and performance of Elmer/Ice, a new-generation ice sheet model. *Geosci. Model Dev.* **6**, 1299–1318 (2013).
64. J. F. Nye, The flow law of ice from measurements in glacier tunnels, laboratory experiments and the Jungfraufirn borehole experiment. *Proc. R. Soc. A.* **219**, 477–489 (1953).
65. J. W. Glen, The creep of polycrystalline ice. *Proc. R. Soc. London. Ser. A. Math. Phys. Sci.* **228**, 519–538 (1955).
66. A. Gilbert, O. Gagliardini, C. Vincent, P. Wagnon, A 3-D thermal regime model suitable for cold accumulation zones of polythermal mountain glaciers. *J. Geophys. Res. Earth Surf.* **119**, 1876–1893 (2014).
67. J. Weertman, On the sliding of glaciers. *J. Glaciol.* **3**, 33–38 (1957).
68. S. J. Cook, P. Christoffersen, J. Todd, A fully-coupled 3D model of a large Greenlandic outlet glacier with evolving subglacial hydrology, frontal plume melting and calving. *J. Glaciol.*, 1–17 (2021).
69. R. Pettersson, P. Jansson, H. Blatter, Spatial variability in water content at the cold-temperate transition surface of the polythermal Storglaciären, Sweden. *J. Geophys. Res. Earth Surf.* **109**, F02009 (2004).
70. C. V. Deutsch, A. G. Journel, *GSLIB : geostatistical software library and user's guide* (Oxford University Press, Oxford, 1998).
71. J.-P. Chiles, P. Delfiner, *Geostatistics : modeling spatial uncertainty* (Wiley, Hoboken, ed. 2nd, 2012).
72. M. Pyrcz, J. Jo, H. Kupenko, A. Liu, A. E. Gigliotti, T. Salomaki, J. E. Santos, GeostatsPy. *GitHub* (2021), (available at https://github.com/GeostatsGuy).
73. M. Pyrcz, C. Deutsh, *Geostatistical Reservoir Modeling* (Oxford University Press, Oxford, ed. 2nd, 2014; https://global.oup.com/academic/product/geostatistical-reservoir-modeling-9780199731442).
74. B. Kulessa, A. L. Hubbard, A. D. Booth, M. Bougamont, C. F. Dow, S. H. Doyle, P. Christoffersen, K. Lindbäck, R. Pettersson, A. A. W. Fitzpatrick, G. A. Jones, Seismic evidence for complex sedimentary control of Greenland Ice Sheet flow. *Sci. Adv.* **3**, e1603071 (2017).
75. V. Baltrūnas, P. Šinkūnas, B. Karmaza, A. Česnulevičius, E. Šinkūnė, The sedimentology of debris within basal ice, the source of material for the formation of lodgement till: an example from the Russell Glacier, West Greenland. *Geologija*. **51**, 12–22 (2009).
76. A. D. Booth, P. Christoffersen, C. Schoonman, A. Clarke, B. Hubbard, R. Law, S. H. Doyle, T. R. Chudley, A. Chalari, *Geophys. Res. Lett.*, in press, doi:10.1029/2020GL088148.
77. C. Hofstede, P. Christoffersen, B. Hubbard, S. H. Doyle, T. J. Young, A. Diez, O. Eisen, A. Hubbard, Physical Conditions of Fast Glacier Flow: 2. Variable Extent of Anisotropic Ice and Soft Basal Sediment From Seismic Reflection Data Acquired on Store Glacier, West Greenland. *J. Geophys. Res. Earth Surf.* **123**, 349–362 (2018).
78. T. P. Lane, D. H. Roberts, C. Ó Cofaigh, B. R. Rea, A. Vieli, Glacial landscape evolution in the Uummannaq region, West Greenland. *Boreas*. **45**, 220–234 (2016).
79. P. R. Dawes, The bedrock geology under the Inland Ice: the next major challenge for Greenland mapping. *GEUS Bull.* **17**, 57–60 (2009).
80. M. Krabbendam, T. Bradwell, Quaternary evolution of glaciated gneiss terrains: pre-glacial weathering vs. glacial erosion. *Quat. Sci. Rev.* **95**, 20–42 (2014).

81. R. B. Alley, K. M. Cuffey, L. K. Zoet, Glacial erosion: Status and outlook. *Ann. Glaciol.* **60**, 1–13 (2019).
82. R. B. Alley, N. Holschuh, D. R. MacAyeal, B. R. Parizek, L. Zoet, K. Riverman, A. Muto, K. Christianson, E. Clyne, S. Anandakrishnan, N. Stevens, A. Smith, R. Arthern, R. Bingham, A. Brisbourne, O. Eisen, C. Hofstede, B. Kulessa, L. Sterns, P. Winberry, J. Bodart, L. Borthwick, E. Case, C. Gustafson, J. Kingslake, H. Ockenden, C. Schoonman, E. Schwans, *J. Geophys. Res. Earth Surf.*, in press, doi:10.1029/2021JF006339.
83. S. Koellner, B. R. Parizek, R. B. Alley, A. Muto, N. Holschuh, The impact of spatially-variable basal properties on outlet glacier flow. *Earth Planet. Sci. Lett.* **515**, 200–208 (2019).

Supplementary material

Table S1. Details for model runs. * Domain center (longitude, latitude in decimal degrees). † Seed used to simulate topography from model variogram, i = 10007, ii = 10009. ‡ From the average of two boreholes drilled at S5 detailed in (*30*). § northeast quarter of RESPONDER domain.

Run (abbreviation)	Location*	Depth (m)	Slope (°)	*F*	Seed†
S5 BedMachine (S5bm)	49.2889 W, 67.2014 N (S5 in (*24*))	818‡	0.8	1.2	NA
S5 geostat a (S5ga)	-	-	1.05	1.2	i
S5 geostat b (S5gb)	-	-		0.9	i
RESPONDER BedMachine (Rbm)	-50.0875 W, 70.5683 N (BH19c in (*58*))	1,043	1.4	1.2	NA
RESPONDER geostat a (Rga)	-	-	1.85	1.2	i
RESPONDER geostat b (Rgb)	-	-	1.775	0.9	i
RESPONDER geostat c (Rgc)	-	-	1.85	1.2	ii
SAFIRE geostat (SAFg)	-49.92 W, 70.52 N (S30 in (*17*))	611		0.9	i
resolution tests	§	1,043	1.775	0.9	i

Table S2. Model parameters. * Value for Sermeq Kujalleq then Isunnguata Sermia

Symbol	Units	Variable	Value	Citation
A_1	MPa a^{-1}	Rate factor 1	9.133e12	
A_2	MPa a^{-1}	Rate factor 2	7.477e23	
A_{lim}	MPa a^{-1}	Limiting rate factor		
A_s	m a^{-1} MPa^{-n}	Sliding coefficient	2.13e4	Average of Helanow et al. (2021) values
C		Maximum slope value	0.16167	Average of Helanow et al. (2021) values
C_a	J kg^{-1} K^{-2}	Enthalpy heat capacity A	7.253	Gilbert et al. (2014)
C_b	J kg^{-1} K^{-1}	Enthalpy heat capacity B	146.3	Gilbert et al. (2014)
E_a	J kg^{-1}	Enthalpy curve parameter a*	1.6155e5 7.5645e4	
E_b	J kg^{-1}	Enthalpy curve parameter b*	-1.5091e5 - 5.8647e4	
E_c	J kg^{-1}	Enthalpy curve parameter c*	1.2341e5 1.1898e5	

G_b	W m^{-2}	Geothermal heat flux	55e-3	Cook et al. (2020)
L	J kg^{-1}	Latent heat of fusion of ice	3.34e4	
κ_c		Cold ice enthalpy diffusivity	1.024e-3	Gilbert et al. (2014)
κ_t		Temperate ice enthalpy diffusivity	1.045e-4	Gilbert et al. (2014)
P_{tr}	MPa	Triple-point pressure of water	0.612	
Q_1		Activation energy 1	60e3	
Q_2		Activation energy 2	115e3	
ρ_i	kg m^{-3}	Ice density	910	
T_{lim}	K	Limit temperature	263.2	Cuffey and Paterson (2010)
T_{ref}	K	Reference temperature	200	
T_{tr}	K	Triple-point temperature of water	273.2	
W_1	MPa a^{-1}	Water viscosity factor 1	1.0	
W_2	MPa a^{-1}	Water viscosity factor 2	2.35	
W_3	MPa a^{-1}	Water viscosity factor 3	77.945	
ω		Upper water limit	0.025	

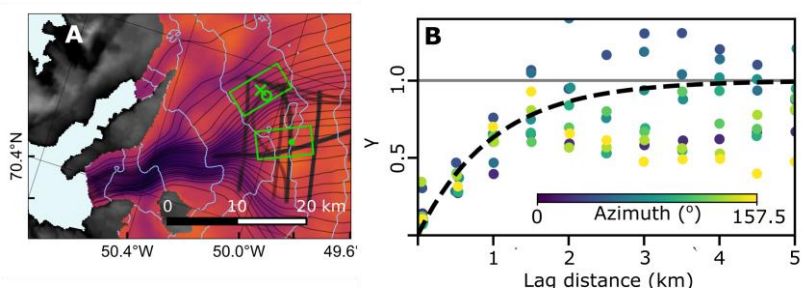

Fig. S1. (**A**) Sermeq Kujalleq showing flowlines in black converging into fjord (pale blue). BedMachine v3 (*14*) basal topography (inferno), land topography (grayscale), and ice surface contours (pale blue). Model domain locations (fluorescent green rectangles) containing RESPONDER BH19c location [fluorescent green cross (*23*)], RESPONDER BH18c location [fluorescent circle (*27*)], SAFIRE BH14b and BH14c locations [fluorescent green dot (*28*)] and radar flight lines for SAFIRE domain [black strokes within dashed boundary, scatter opacity means darker lines have more measurements, (*29*)]. (**B**) modeled variogram (dashed line) and empirical variograms for varying azimuths (scatter points) for SAFIRE domain.

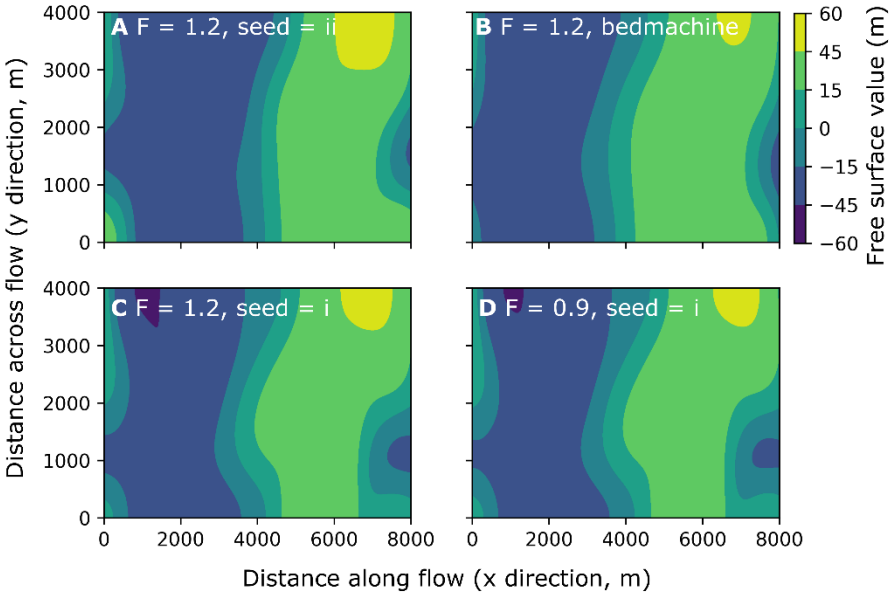

Fig. S2. Free surface variation for RESPONDER runs (**A**) Rgc, (**B**) Rbm, (**C**) Rga, and (**D**) Rgb.

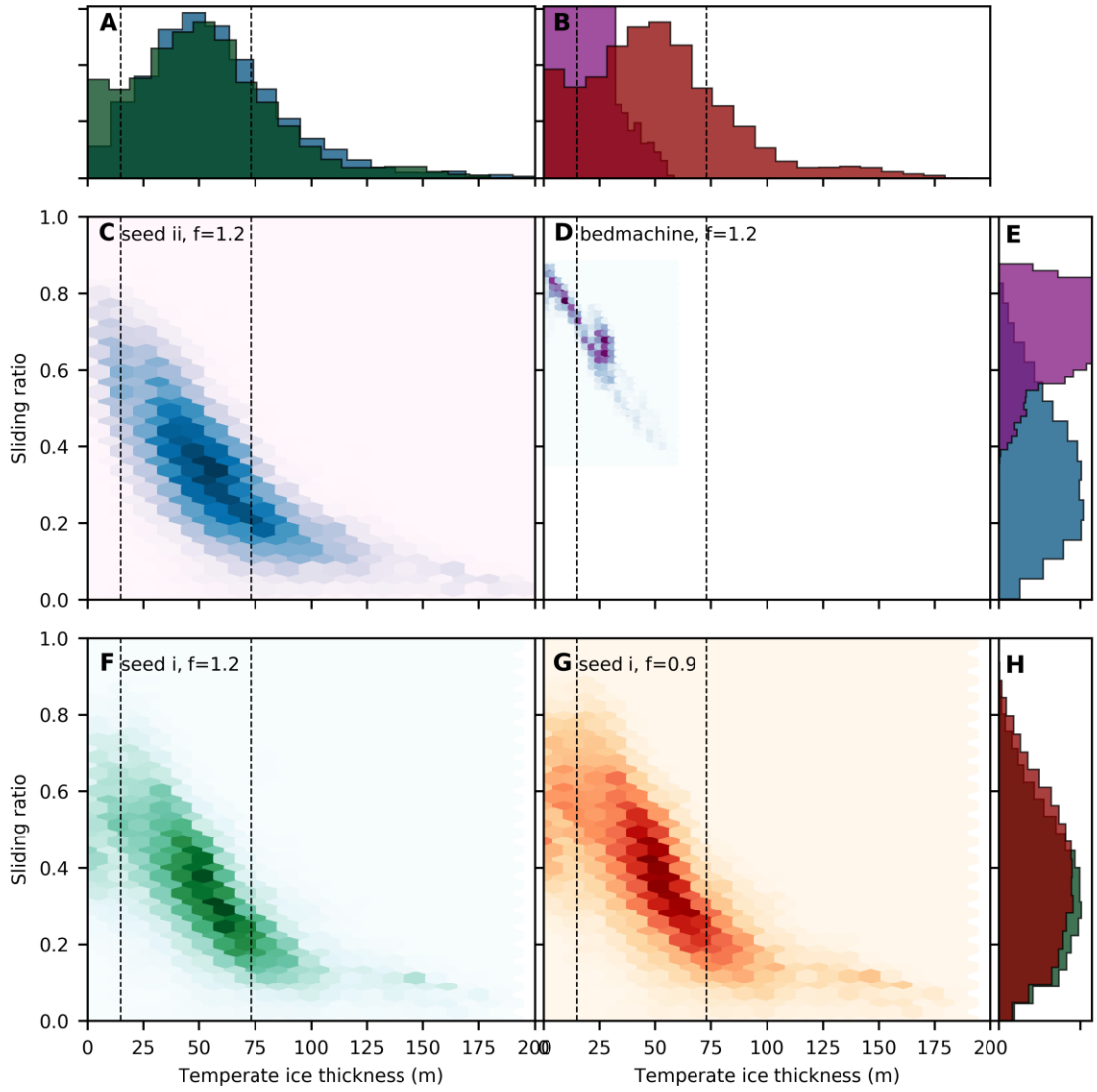

Fig. S3. Hexbins and histograms for four RESPONDER domain runs. Panel details refer to run details. (**C**) = Rgc, (**D**) = Rbm, (**F**) = Rga, (**G**) = Rgb.

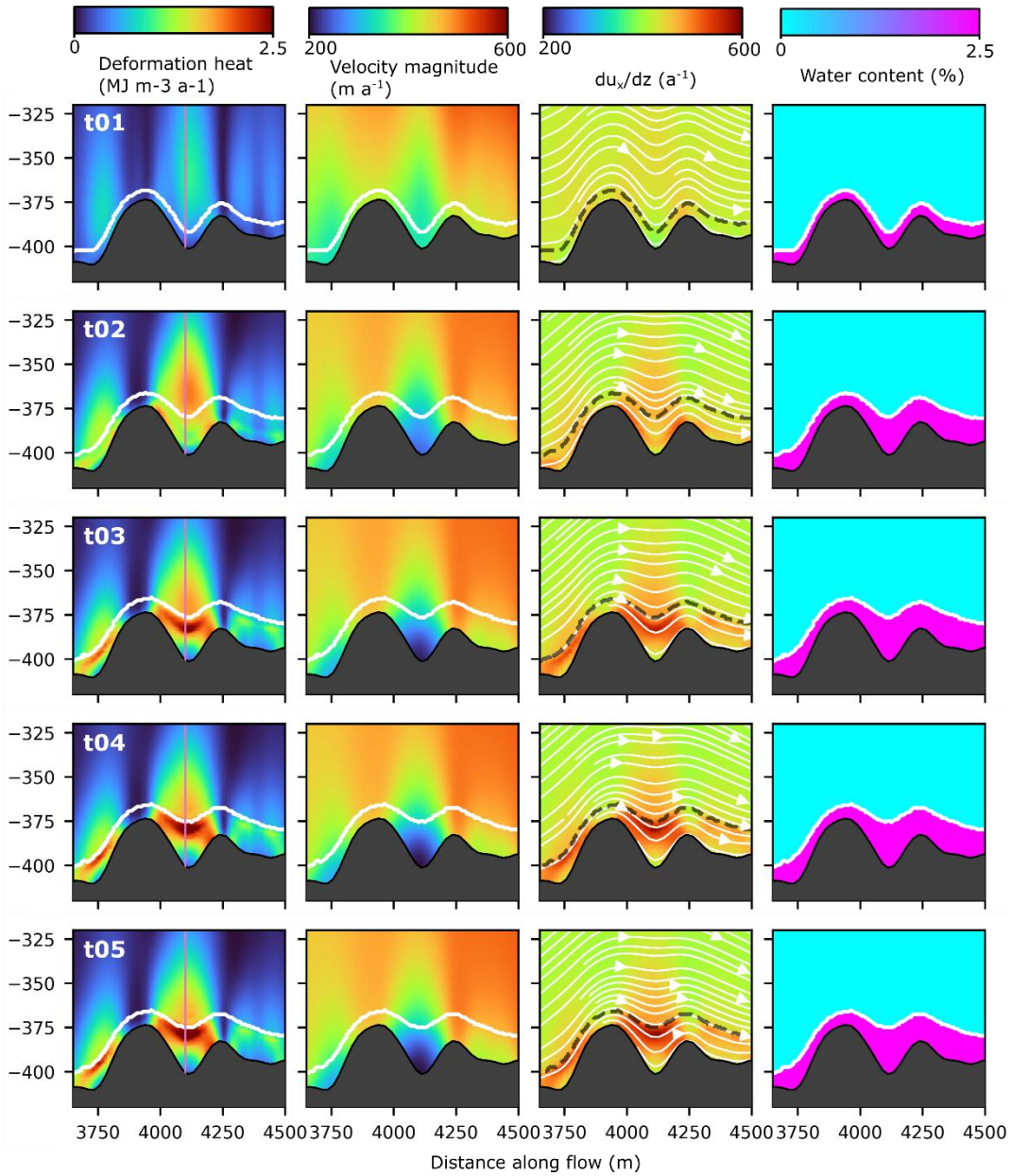

Fig. S4. Evolution towards steady state for deformation heat (column 1), velocity magnitude (column 2), change in x velocity component with height (column 3), and water content (column 4) for the five iterations (rows) required for steady state for the close-up in Fig. 5.

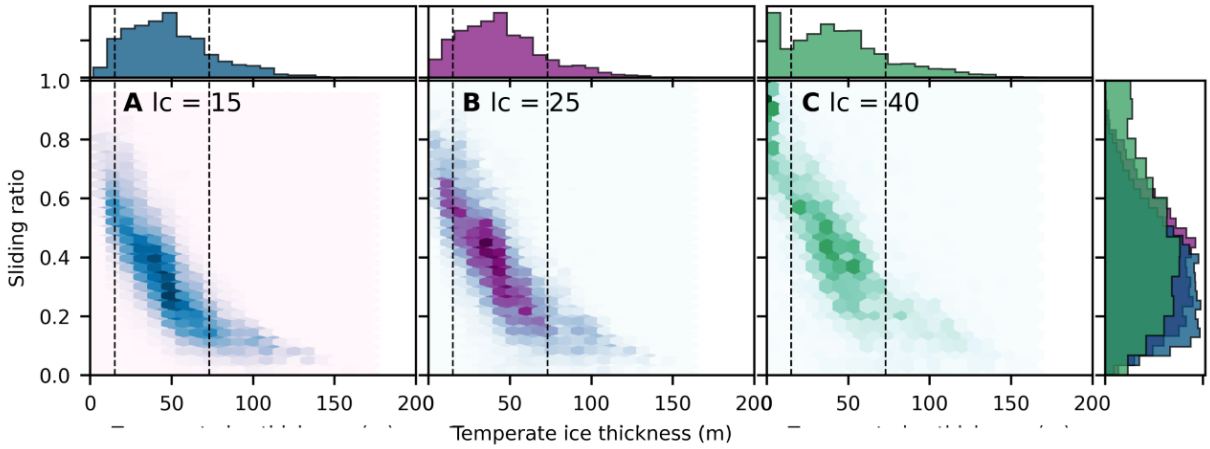

Fig. S5. Hexbins and histograms for representative element length (lc) of 15, 25, and 40 m (A, B, and C respectively). These show minor difference between lc = 15 m and lc = 25 m, with notable increases in temperate ice in the lowest-thickness bin, and high basal velocity ratios for lc = 40 m.

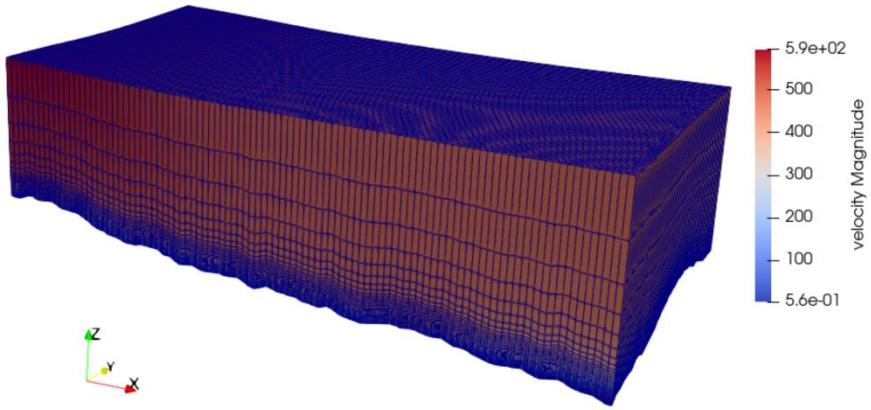

Fig. S6. Domain used in resolution tests, here with lc = 40. Dimensions are 2 km across flow, 4 km along flow, depth ~1,043 m. This is the bottom left corner of the full RESPONDER seed i domain as viewed from above.

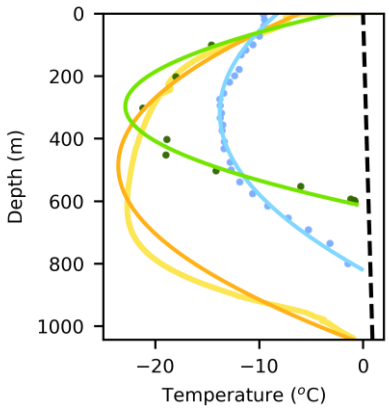

Fig S7. Temperature profiles with fitted curves for Sermeq Kujalleq (orange) and Isunnguata Sermia (sky blue). Yellow line is from BH19c (*23*), blue scatter is from S5 (*30*). Black dashed line is the pressure melting point using a Clausius-Clapeyron slope of 0.0974 K MPa^{-1}.

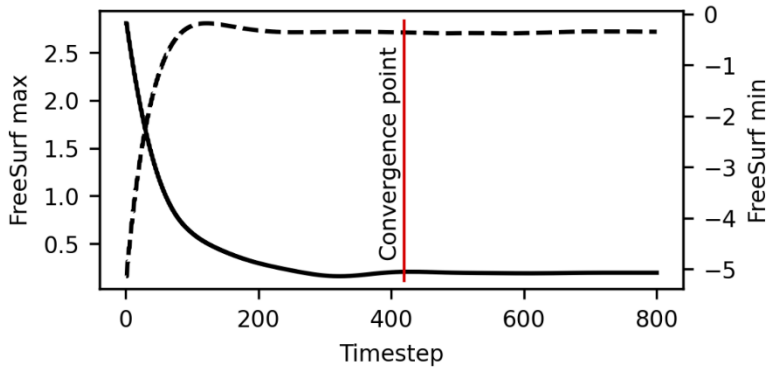

Fig S8. Change in free surface max (dashed line) and min (solid line) values with time including point where the model is deemed to have converged.

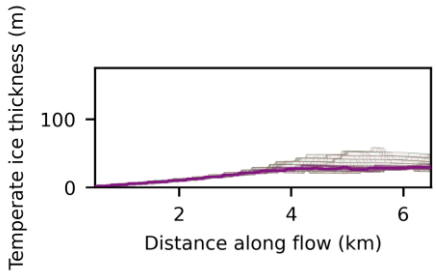

Fig S9. Basal temperate layer ice thickness averaged across flow for the RESPONDER domain forced with BedMachine topography (Run Rbm).

Supplementary text, geological considerations

Individual GrIS glacier catchments are often assumed to be underlain by either hard crystalline bedrock or soft sediments. However, this assumption rests on a paucity of data constraining the physical characteristics of the ice-bed interface. Collection of new GrIS field data over the last decade suggests a more complicated situation, with no clear consensus for blanket hard- or soft-bed settings. At Isunnguata Sermia, borehole data mostly from topographic highs (sites S1-S5) suggests hard-bed conditions (*61*), while seismic surveys from topographic depressions indicate deformable sediment (*60*, *74*), and ice-marginal studies for the nearby Russell Glacier indicate basal ice with a high debris content (*75*). At Sermeq Kujalleq, distributed acoustic sensing data from BH19c and seismic surveys across the SAFIRE domain both suggest a layer of sediment (*76*, *77*), yet ice-marginal glacial geology is dominated by areal scour with limited and isolated zones of sediment deposition (*78*). Furthermore, the crystalline Precambrian rock over which both our domains probably lie (*79*) typically exhibits a ‘cnoc-and-lochan’ landscape in deglaciated areas – characterized by overdeepened glacier-eroded rock basins and knolls with amplitudes up to 100 m (*57*, *80*) – as broadly recreated in our geostatistical simulations (Fig. 1).

Our understanding of subglacial transport processes remains poorly quantified (*81*), but we suggest that realistically rough topography, and a variable basal stress/velocity field as produced in our model, are likely to result in heterogeneous sediment distribution and hence heterogeneous basal traction characteristics. High slip rates and basal traction over topographic highs are likely to lead to high rates of erosion, meaning these regions are most likely composed of hard bedrock. Conversely, topographic lows may act as sites of sediment accumulation through basal melt-out, lower bed-normal pressure (*82*) and slower glacier motion. This has important implications for basal motion. Although topographic prominences occupy a small overall area they are sites of high basal-slip and the traction at these locations will exert a disproportionate control on basal

motion. This variation may explain the success of hard-bed Weertman-style basal-slip relationships across the GrIS when viewed at >1 km scales (*51*) even when more recent studies suggest a regularized-Coulomb approach is more applicable (*26*), particularly if the viscous flow of temperate ice is contributing a considerable proportion of overall motion. Models investigating spatial variation in basal-traction relationships, similar to (*83*) but also incorporating realistic topography, will shed further light on these processes.

Basal freeze on

In order to hold the basal temperature constant at the melting point the following energy consideration must be met

$$\rho \frac{\partial H}{\partial t} = -\frac{\partial q}{\partial z} + \gamma = \kappa_c \frac{\partial^2 H}{\partial z^2} + \gamma = 0 \quad \text{(S1)}$$

where q is vertically directed energy flux into the ice and γ accounts for other sources of energy supplied to the bed

$$\gamma = F_b + G_b + Q_b + VHD + \rho V_b L \quad \text{(S2)}$$

where Q_b is water transport, VHD is viscous heat dissipation (*42*), and V_b is the basal freeze on rate of liquid water. Neglecting terms other than $\rho V_b L$ then gives

$$\rho V_b L = \kappa_c \frac{\partial^2 H}{\partial z^2} \quad \text{(S3)}$$

and, setting the right hand side to 2.7e-4 (the largest value from the borehole profile of (*23*)(*21*)) gives V_b = 2.8e-5 m a^{-1}, negligible in the context of high basal melt rates modeled across the domain.